

1 **Single-Soma Deep RNA Sequencing of Human Dorsal Root Ganglion Neurons Reveals**  
2 **Novel Molecular and Cellular Mechanisms Underlying Somatosensation**

3 Huasheng Yu<sup>1</sup>, Dmitry Usoskin<sup>2\*</sup>, Saad S. Nagi<sup>3\*</sup>, Yizhou Hu<sup>2</sup>, Jussi Kupari<sup>2</sup>, Otmane  
4 Bouchatta<sup>3</sup>, Suna Li Cranfill<sup>1</sup>, Mayank Gautam<sup>1</sup>, Yijing Su<sup>1</sup>, You Lu<sup>1</sup>, James Wymer<sup>4</sup>, Max  
5 Glanz<sup>4</sup>, Phillip Albrecht<sup>5</sup>, Hongjun Song<sup>1</sup>, Guo-Li Ming<sup>1</sup>, Stephen Prouty<sup>6</sup>, John Seykora<sup>6</sup>, Hao  
6 Wu<sup>7</sup>, Minghong Ma<sup>1</sup>, Frank L Rice<sup>5</sup>, Håkan Olausson<sup>3#</sup>, Patrik Ernfors<sup>2#</sup>, Wenqin Luo<sup>1#</sup>

7 1. Department of Neuroscience, Perelman School of Medicine, University of Pennsylvania, Phil-  
8 adelphia, PA 19104, USA.

9 2. Department of Medical Biochemistry and Biophysics, Division of Molecular Neurobiology,  
10 Karolinska Institute, Stockholm 17177, Sweden.

11 3. Department of Biomedical and Clinical Sciences, Linköping University, Linköping 58185,  
12 Sweden.

13 4. Department of Biochemistry and Molecular Biology, College of Medicine, University of Flor-  
14 ida, Gainesville, FL 32603, USA.

15 5. Neuroscience & Pain Research Group, Integrated Tissue Dynamics, LLC, Rensselaer, NY  
16 12144, USA.

17 6. Department of Dermatology, Perelman School of Medicine, University of Pennsylvania, Phil-  
18 adelphia, PA 19104, USA.

19 7. Departments of Genetics, Perelman School of Medicine, University of Pennsylvania, Phila-  
20 delphia, PA 19104, USA

21 \* These authors contributed equally to this work

22 # Correspondence:

23 [hakan.olausson@liu.se](mailto:hakan.olausson@liu.se) (Håkan Olausson)

24 [patrik.ernfors@ki.se](mailto:patrik.ernfors@ki.se) (Patrik Ernfors)

25 [luow@penntmedicine.upenn.edu](mailto:luow@penntmedicine.upenn.edu) (Wenqin Luo)

26

27

28

29

30

31

32

33

34

35

36

37

38

39

40

41

42

43

44

45

46

47 **Abstract:**

48 The versatility of somatosensation arises from heterogeneous dorsal root ganglion (DRG) neu-  
49 rons. However, soma transcriptomes of individual human DRG (hDRG) neurons – critical in-  
50 formation to decipher their functions – are lacking due to technical difficulties. Here, we devel-  
51 oped a novel approach to isolate individual hDRG neuron somas for deep RNA sequencing  
52 (RNA-seq). On average, >9,000 unique genes per neuron were detected, and 16 neuronal types  
53 were identified. Cross-species analyses revealed remarkable divergence among pain-sensing neu-  
54 rons and the existence of human-specific nociceptor types. Our deep RNA-seq dataset was espe-  
55 cially powerful for providing insight into the molecular mechanisms underlying human  
56 somatosensation and identifying high potential novel drug targets. Our dataset also guided the  
57 selection of molecular markers to visualize different types of human afferents and the discovery  
58 of novel functional properties using single-cell *in vivo* electrophysiological recordings. In sum-  
59 mary, by employing a novel soma sequencing method, we generated an unprecedented hDRG  
60 neuron atlas, providing new insights into human somatosensation, establishing a critical founda-  
61 tion for translational work, and clarifying human species-specific properties.

62

63

64

65

66

67

68

69

70 **Introduction:**

71 The somatosensory system conveys senses, such as temperature, touch, vibration, and body posi-  
72 tion<sup>1</sup>. Primary somatosensory neurons, which convert stimuli to electrical signals, are located in  
73 the dorsal root ganglia (DRG) and trigeminal ganglia (TG)<sup>2</sup>. They are greatly heterogeneous,  
74 composed of many different molecularly and functionally distinct populations<sup>3</sup>. Somatosensation  
75 is fundamental to our daily lives, but becomes a devastating human health problem when mal-  
76 functioning, such as during chronic pain and itch. Safe and effective drug options for chronic  
77 pain and itch are still limited<sup>4-6</sup>, and the development of novel treatment strategies is greatly  
78 needed.

79

80 Most of our current knowledge about the mammalian somatosensory system has been obtained  
81 from model organisms, mainly rodents. However, the success rate of translating treatment strate-  
82 gies working in model organisms such as rodents to humans has been low<sup>7,8</sup>. There may be mul-  
83 tiple reasons for the lack of success, but a noticeable one is species differences of the genetic,  
84 molecular and potentially even cellular makeup of somatosensory neurons between rodents and  
85 humans. Some significant differences between rodent and human DRG (hDRG) neurons have  
86 been noticed in previous studies, with neuropeptides, ion channels, and other markers not always  
87 matching between the species<sup>9,10</sup>. For an example, MRGPRX4, a bile acid receptor for human  
88 cholestatic itch, does not have a molecular ortholog in mice<sup>11</sup>. In contrast, TGR5, a receptor  
89 identified in mouse DRG neurons for bile acid-induced itch<sup>12</sup>, is not expressed in hDRG neurons  
90 but instead in the surrounding satellite glial cells<sup>11</sup>. Thus, it is critical to elucidate molecular pro-  
91 files and cell types of hDRG neurons for understanding human somatosensory mechanisms as  
92 well as for translational purposes.

93

94 Single-cell RNA sequencing (RNA-seq) is a powerful tool to qualitatively and quantitatively  
95 study transcripts of individual cells (soma and/or nuclei)<sup>13</sup>. Based on the transcriptome, including  
96 both transcript identities and expression levels, heterogenous cells can be classified into different  
97 types<sup>14</sup>. This approach has been successfully used in varying degrees to study DRG and TG neu-  
98 rons in mouse, macaque and other model organisms<sup>15-18</sup>, providing comprehensive molecular and  
99 cellular atlases for understanding somatosensory neurons and their differentiation. However,  
100 there are some unique technical challenges for conducting single-cell RNA-seq of human DRG  
101 or TG neurons: 1) Human tissues are more difficult to obtain compared to model organisms, and  
102 the quality of human tissues (RNA integrity) is much more variable; 2) In human DRG/TG tis-  
103 sues, non-neuronal cells, including satellite glial cells, fibroblasts, and other cell types, greatly  
104 outnumber the neuronal cells<sup>9,19</sup>; 3) Satellite glial cells tightly wrap around neuronal somas<sup>9,19</sup>,  
105 making their physical separation difficult; 4) Human DRG/TG neuronal somas are much larger  
106 than those of mouse DRG/TG neuronal somas, so they are prone to damage by enzyme digestion  
107 and mechanical forces during single-cell isolation and not compatible with many current se-  
108 quencing platforms. In addition, transcriptome changes caused by enzymatic and mechanical  
109 dissociation may also affect cell clustering and cell type identification<sup>20</sup>. Due to these difficulties,  
110 single-nucleus RNA-seq and 10x Visium spatial transcriptomics have been employed for human  
111 DRG/TG neurons<sup>21-24</sup>. Despite novel insights from these studies, the quantity of transcripts in the  
112 nucleus is much lower than those in the soma, and the nuclear transcripts may not represent the  
113 full transcriptome profile of the whole cell<sup>25</sup>, while the 10x Visium spatial transcriptomics lack  
114 single-neuron resolution (Fig. 1A). Thus, it is necessary to develop a new method that enables  
115 soma RNA-seq of hDRG neurons while preserving the single-cell resolution.

116

117 To meet this challenge, we developed a novel approach by combining laser capture  
118 microdissection (LCM) for isolating individual neuronal somas and the Smart-seq2<sup>18</sup> for generat-  
119 ing full length RNA-seq libraries (Fig. 1A). We sequenced 1066 hDRG neurons with minimum  
120 satellite glial cell contamination from six lower thoracic and lumbar DRGs of three donors, de-  
121 tecting an average of >9,000 unique genes per neuron (~ 3-5 times or more than the previous  
122 single-nucleus RNA-seq results) and identifying 16 molecularly distinctive neuron types. Cross-  
123 species analysis revealed both similarities but considerable differences among human, macaque,  
124 and mouse DRG neurons. In addition, we uncovered a set of novel marker genes that can help to  
125 distinguish different types of sensory neurons and afferents in hDRG and skin tissues. Based on  
126 the molecular profiles, we also predicted novel response properties of human sensory afferents,  
127 which were tested and confirmed by single-cell *in vivo* recordings. These results support a close  
128 relationship between the molecular profiles uncovered by single-soma RNA-seq, histology, and  
129 functional properties of human sensory afferents, highlighting the precision and unique utility of  
130 this dataset in guiding functional studies of human somatosensory neurons. In short, we have  
131 established a novel approach to conduct single-soma deep RNA-seq of hDRG neurons, which  
132 revealed previously unknown neuronal types and functional properties. Given the high number  
133 of unique transcripts recovered from each neuron, our dataset is especially powerful for molecu-  
134 lar discovery, such as identifying potential high value novel drug targets. We believe that this  
135 high-fidelity single-soma RNA-seq dataset will serve as a ground reference for homogenizing  
136 RNA-seq data of human DRG/TG neurons using different approaches and for translating animal  
137 studies into therapeutic applications.

138

139 **Results**

140 **Development of an LCM-based approach for conducting single-soma deep RNA-seq of**  
141 **human DRG neurons**

142 Adult human DRG neurons present considerable technical challenges for high-quality single-cell  
143 RNA-seq study. To overcome these hurdles, we developed a novel method that utilizes the laser  
144 capture microdissection to isolate individual neuronal soma and combine with Smart-seq2 full  
145 length RNA-seq library generation method for single-soma high-depth transcriptomic analysis  
146 (Fig. 1A). Six hDRGs at the low thoracic (T11-T12) and lumbar (L2-L5) levels from three post-  
147 mortem donors (donor information and screening criteria are summarized in the supplementary  
148 tables 1 & 2) were procured through NDRI (National Disease Research Interchange). DRGs  
149 were extracted and immediately frozen in OCT (within ~ 6 hours after death) at the NDRI pro-  
150 curement sites to minimize RNA degradation. Fresh frozen DRGs were cryo-sectioned, mounted  
151 onto LCM slides, and briefly stained with a HistoGene<sup>TM</sup> dye for cell visualization (Fig. S1A-C).  
152 Individual neuronal somas were discernable under microscope and dissected by a laser (Fig. 1A).  
153 Each detached soma dropped into a tube cap containing cell lysis buffer for library preparation  
154 (Fig. 1A). Dissected neuronal somas exhibited a similar size distribution as the whole DRG neu-  
155 ron population (Fig. S1D-E), suggesting no obvious sampling bias. Sequencing libraries were  
156 generated following the Smart-seq2 protocol<sup>26</sup>. In total, 1136 neuronal somas were dissected and  
157 passed through the final quality control for sequencing. During preliminary bioinformatic analy-  
158 sis, 70 samples with obvious glial cell contamination (dominant expression of APEO, FABP7,  
159 and other glia cell markers) were removed, and the remaining 1066 neurons were used for analy-  
160 sis in this study. 16 transcriptomic clusters of hDRG neurons were identified by Seurat<sup>27</sup> (Fig.  
161 1B), with an average of 9486 genes detected per cell (Fig. 1C). No obvious batch effects or do-

162 nor differences were observed in the clusters (Fig. S2A-E). All these cells expressed high levels  
163 of known peripheral sensory neuronal markers, *SLC17A6* (*VGLUT2*), *SYP* (Synaptophysin), and  
164 *UCHL1* (*PGP9.5*) (Fig. 1D, S2F-G).

165

166

### 167 **Anatomical and molecular features of hDRG neuron clusters**

168 Mammalian DRG neurons have some well-known physiological, anatomical, and molecular fea-  
169 tures. DRG somatosensory afferents can be identified as A- or C- afferent fibers according to  
170 axon conduction velocities<sup>28</sup>. A-fiber DRG neurons usually have large-diameter somas and  
171 myelinated axons, while C-fiber DRG neurons have small-diameter somas and non-myelinated  
172 axons. The A- and C- afferents can be further divided into peptidergic and non-peptidergic types,  
173 based on the expression of one neuropeptide, calcitonin related polypeptide alpha  
174 (*CALCA*(*CGRP*))<sup>29</sup>. To determine the broad types of the 16 hDRG neuron clusters, we analyzed  
175 their soma sizes and expression of some key molecular markers (Fig. 1E). Clusters 1-16 were  
176 arranged from small to large soma sizes. In addition, expression of neurofilament intermediate  
177 filament (*INA*), which was enriched in small-diameter DRG neurons, and heavy chain (*NEFH*),  
178 which was highly expressed in large-diameter DRG neurons, showed a clear complementary  
179 pattern. The combined morphological and molecular features suggested that clusters 1-7 were  
180 likely to be unmyelinated, small diameter C-fiber DRG neurons, whereas clusters 8-16 were  
181 myelinated, large diameter A-fiber DRG neurons (Fig. 1E). The two groups could be further di-  
182 vided based on the expression of *CALCA* (clusters 5-12). Moreover, the PR domain zinc finger  
183 protein 12 (*PRDM12*), a transcriptional regulator critical for development of human pain-sensing  
184 afferents (nociceptors) and C fibers<sup>30</sup>, was expressed in clusters 1-12, further distinguishing be-

185 tween C- and A-fiber nociceptors versus A-fiber low-threshold mechanoreceptors (Fig. 1E).  
186 Taken all information into consideration, clusters 1-4 were classified as non-peptidergic C-fibers,  
187 clusters 5-7 as peptidergic C-fibers, clusters 8-12 as peptidergic A-fibers, clusters 13-15 as low-  
188 threshold mechanoreceptors A-fibers (A-LTMRs), and cluster 16 as an unknown A-fiber type  
189 (Fig. 1E).

190  
191 Based on the expression profiles of top molecular markers, which had either unique expression  
192 pattern or well-known functions (Fig. 1F, S2H), we named these 16 hDRG neuron clusters using  
193 a nomenclature system with the following format (Fig. 1G): 1) The “h” at the beginning of each  
194 cluster name indicated “human”; 2) mouse nomenclature was used for conserved subtypes (i.e.  
195 most non-peptidergic neurons and A-LTMRs); 3) human peptidergic neuron types were desig-  
196 nated as hPEP.(marker gene). Briefly, for non-peptidergic C-fiber neurons, cluster 1 was named  
197 hTRPM8, cluster 2 was C-fiber low-threshold mechanoreceptors (hC.LTMR), cluster 3 was type  
198 I non-peptidergic nociceptors (hNP1), and cluster 4 was type II non-peptidergic nociceptor  
199 (hNP2). For peptidergic C-fiber neurons, cluster 5 was named hPEP.SST, cluster 6  
200 hPEP.TRPV1/A1.1, and cluster 7 hPEP.TRPV1/A1.2. For peptidergic A-fiber neurons, cluster 8  
201 was named hPEP.PIEZO<sup>h</sup> (the superscript ‘h’ means ‘high’), cluster 9 hPEP.KIT, cluster 10  
202 hPEP.CHRNA7, cluster 11 hPEP.NTRK3, and cluster 12 hPEP.0 (no distinctive molecular  
203 marker). For A-LTMRs, cluster 13 was named A $\delta$  low-threshold mechanoreceptors  
204 (hA $\delta$ .LTMR), cluster 14 A $\beta$  low-threshold mechanoreceptors (hA $\beta$ .LTMR), and cluster 15 pro-  
205 prioceptors (hPropr). Cluster 16 was named hATF3.

206

207 To validate the clusters identified by Seurat analysis, we independently analyzed our data using  
208 the graph-based clustering Conos<sup>31</sup> package. Cluster structure revealed by Conos analysis repro-  
209 duced the Seurat results (Fig. S3A). As a third method to validate identified clusters, we em-  
210 ployed a neural network-based probabilistic scoring module<sup>15,18</sup> that learned human cell type  
211 features based on their molecular profiles (Fig. S3B-D). Namely, the accuracy score of our Seu-  
212 rat clustering assignment by the learning module was near 90% (Fig. S3B), which meant that  
213 most cells were accurately assigned to their corresponding clusters, confirming the accuracy of  
214 clustering (Fig. S3C). Moreover, the cell type consistency was validated by probabilistic simi-  
215 larity (Fig. S3D). Thus, three independent analysis methods confirmed the robustness of the clus-  
216 tering and strongly supported the cell type assignment.

217  
218 Using Conos we also performed co-clustering and label propagation with a recently published  
219 single-nucleus RNA-seq dataset of hDRG neurons by Nguyen et al<sup>23</sup> (Fig. S4). This analysis  
220 showed that while some clusters displayed a one-to-one match between the two datasets, such as  
221 hTRPM8, hPEP.SST, hPEP.KIT, and hAd.LTMR, most did not have one-to-one match. This  
222 mismatch could be caused by biological variations such as nucleus vs cytoplasm RNA species  
223 and quantity<sup>25</sup> and technical differences (the increased resolution obtained by deep sequencing in  
224 the present study or variability caused by the different technology platforms<sup>26,32</sup>). This mismatch  
225 also indicated that our dataset generated novel molecular profiles and cell types different from  
226 the single-nucleus RNA-seq results.

227

228

229 **Cross-species comparison of DRG neuron types**

230 Comparison of hDRG neuron types to those in model organisms helps to uncover the evolutionary  
231 conservation and divergence of DRG neuron populations, provides clues about functions of  
232 hDRG neuron populations, and identifies potential species-specific hDRG neuron populations.  
233 Here we performed a cross-species comparison between our human dataset, a mouse dataset  
234 (Sharma)<sup>16</sup>, and a macaque dataset (Kupari, SmartSeq2 dataset)<sup>18</sup>. To identify corresponding  
235 clusters between human and previously published mouse and macaque datasets, we used three  
236 different strategies: Conos pairwise co-clustering followed by label propagation (Fig. 2A-B &  
237 S5A-B), probabilistic neural network learning (Fig. S5C-D), and machine-learning based hierar-  
238 chical clustering of an integrated dataset of human and macaque (Fig. S5E). For characteristics  
239 and details of different approaches, see Method section. In all these analyses, human non-PEP  
240 DRG neuron cell types showed high correlation to those of mouse and macaque, including  
241 hC.LTMR, hNP1, hNP2, hPEP.SST (called NP3 in mouse and monkey), hTRPM8, hA $\delta$ .LTMR,  
242 hA $\beta$ .LTMR, and hProprioceptor neurons (Fig. 2A-B & S5). hPEP.TRPV1/A1.1 and  
243 hPEP.TRPV1/A1.2 corresponded to macaque PEP1 (Usoskin nomenclature) and mouse subclass  
244 PEP1.4/CGRP- $\epsilon$ . This conclusion was supported by both Conos label propagation analysis (Fig.  
245 2A-B) and probabilistic neural network analysis (Fig. S5C-D), suggesting that these clusters to  
246 represent C-fiber thermoreceptors and nociceptors. Notably, four types of mouse C-fiber PEP  
247 (CGRP) nociceptors have been evidenced<sup>18,33</sup> (nomenclature from Emory & Ernfors/Sharma),  
248 but our analysis indicated that mouse clusters PEP1.1/CGRP- $\alpha$ , PEP1.2/CGRP- $\beta$ , and  
249 PEP1.3/CGRP- $\gamma$  might not be evolutionarily conserved, as they did not have equivalent types in  
250 the human datasets (Fig. 2A & S5C). hPEP.CHRNA7 showed high correlation to mouse  
251 PEP2/CGRP- $\zeta$  and macaque PEP2, while hPEP.KIT corresponded to mouse PEP3/CGRP- $\eta$  and  
252 macaque PEP3, suggesting these clusters functionally belong to A-fiber nociceptors (Fig. 2A-B

253 & S5C-D). Interestingly, hPEP.NTRK3, hPEP.PIEZO<sup>h</sup>, and hPEP.0, which made about half of  
254 human PEP nociceptors that we sequenced, did not have a one-to-one corresponding cell types in  
255 either mouse or macaque (Fig. 2A-B & S5C-D). Since macaque PEP2 cluster in the high-quality  
256 Smart-Seg2 macaque dataset contained only three neurons, we focused our interpretation on  
257 analyses on mouse homologs for this cell type. hPEP.NTRK3 showed the greatest similarity to  
258 mouse PEP2 (CGRP- $\zeta$ ) by Conos propagation analysis (Fig. 2A). Probabilistic neural network  
259 learning revealed similar scores to both mouse PEP2 (CGRP- $\zeta$ ) and PEP3 (CGRP- $\eta$ ) (Fig. S5C).  
260 Overall, it therefore seems that hPEP.NTRK3 represents a convergent mouse PEP2/3-like cell  
261 type. hPEP.PIEZO<sup>h</sup> showed some similarity to mouse PEP3 (CGRP- $\eta$ ) and macaque PEP1 and  
262 PEP3 in co-clustering (Fig. 2A-B). Neural network learning, and hierarchical clustering, indicat-  
263 ing this cell type to represent an A-fiber mechanosensory nociceptor (Fig. S5C-E). Thus,  
264 hPEP.NTRK3 and hPEP.PIEZO<sup>h</sup> represents diverged PEP2- and PEP3-like A-fiber nociceptors,  
265 which likely have emerged as human species-specific sensory neuron types. hPEP.0, a type of  
266 human PEP A-afferents, showed no similarity to any mouse DRG neurons but some relationship  
267 to macaque PEP1 and PEP3 (Fig. 2A-B), suggesting that they might be primate specific PEP  
268 nociceptors. A schematic overview of our conclusions based on the above analyses regarding the  
269 cell-type homologs across mouse-macaque-human is illustrated in Fig. 2C.

270  
271 Transcription factors play critical role in DRG neuron development and differentiation<sup>34</sup>. Thus,  
272 we performed a transcription factor associated gene regulatory network analysis (TF-GRNs) us-  
273 ing machine learning to identify shared and species-specific TF-GRNs contributing to the simi-  
274 larities and differences between sensory neuron subtypes and species (Fig. 2D). Evolutionarily  
275 conserved TF-GRNs defining C-fiber nociceptors, A-fiber nociceptors, A-LTMRs, TRPM8, C-

276 fiber pruriceptors/nociceptors (hNP1, hNP2, hPEP.SST), and C-LTMRs were observed (yellow  
277 boxes in Fig. 2D) as well as species-specific networks, such as for C-fiber nociceptors, hTRPM8,  
278 hNP1, hNP2, hPEP.SST and hC.LTMR (green boxes in Fig. 2D). Among cross-species con-  
279 served transcriptional regulators, some were previously known to drive sensory neuron diversifi-  
280 cation in mouse, including *ZEB2* in C-fiber nociceptors<sup>35</sup>, *SHOX2* in A-LTMRs<sup>36,37</sup>, *RUNX3* in  
281 proprioceptors<sup>38</sup>, *FOXP2* in TRPM8, *RUNX1* in NP1<sup>39</sup>, *ZNF52* and *POU4F2* in C-LTMRs<sup>16,40</sup>.  
282 These transcription factors may contribute to the formation of different DRG neuron cell types  
283 and regulate the conserved and species-specific gene expression in each cell population.

284

285

### 286 **Similarities and differences of top marker genes across species**

287 To reveal molecular differences among the corresponding cell types in human, macaque  
288 (Kupari)<sup>18</sup>, and mouse (Sharma)<sup>16</sup>, we selected the top 10 marker genes from each hDRG neuron  
289 population and compared them across species (Fig. S6). In general, the expression patterns of  
290 these genes were more similar between human and macaque than between human and mouse,  
291 reflecting the evolutionary distances between rodent, non-human primate, and human. Some  
292 genes were expressed in the corresponding populations across all three species. For example,  
293 *TRPM8* was expressed in C-fiber cold-sensing neurons, and *IL31RA* was expressed in nocicep-  
294 tive/pruriceptive population (NP3) as well as its corresponding human population hPEP.SST.  
295 Some genes, such as *KCNVI*, a voltage-gated potassium channel, were specific for primate  
296 A $\delta$ .LTMR but had low or no expression in the corresponding mouse DRG neurons (Fig. S6).  
297 Moreover, some marker genes were specific only for hDRG neuron types. For example,  
298 Mechanosensory Transduction Mediator Homolog (*STUM*) was specifically expressed in

299 hTRPM8, and calsequestrin 2 (*CASQ2*) was specifically expressed in hC.LTMR (Fig. S6). Genes  
300 specifically enriched in hDRG neurons may confer unique physiological and functional proper-  
301 ties of the human somatosensory system. The observed differences from the top 10 marker genes  
302 represent only the iceberg tip of the overall molecular differences between human and model  
303 organism DRG neurons, highlighting the necessity of validating molecular targets in hDRG neu-  
304 rons for translational studies.

305

306

### 307 **Molecular marker expression and validation of C-fiber pruriceptors, thermoreceptors and** 308 **nociceptors**

309 Based on the sequencing results, we established specific marker genes or their combination to  
310 identify each type of hDRG neurons (Fig. S7A) and validated their expression using  
311 RNASCOPE multiplex fluorescent *in situ* hybridization (FISH) (Fig. S8). We also deduced po-  
312 tential functions of each hDRG neuron type based on the cross-species cell type comparison and  
313 expression of molecules with known sensory functions.

314

315 hNP1 and hNP2 exclusively expressed *MRGPRX1* (Fig. 3A), a Mas-related GPCR family mem-  
316 ber that could be activated by various pruritogens<sup>41</sup>. Similarly, primate specific bile acid receptor  
317 *MRGPRX4* for mediating human cholestatic itch<sup>11,42</sup> were detected by our single-soma dataset.  
318 Enrichment of *MRGPRX4* and *MRGPRX3* (an orphan GPCR in the same family) in hNP2 but not  
319 hNP1 helped to separate these two clusters (Fig. S7A). Other itch-related receptors, such as  
320 *HRHI* and *IL31RA* (Fig. 3A-B), were also expressed in both hNP1 and hNP2, suggesting that  
321 these two populations function to detect various pruritogens and transmit the sensation of itch.

322 The co-expression of *MRGPRX1* and *HRHI* was validated by multiplex FISH (Fig. 3A). *PIEZO2*  
323 was expressed at a higher level in hNP1 than in hNP2 neurons (Fig. S7B), suggesting that hNP1  
324 neurons could be more mechanosensitive. Consistent with this molecular feature, recordings  
325 from human afferents have revealed that some human histaminergic itch-sensing fibers are  
326 mechanosensitive<sup>43</sup>. In mice, NP1 and NP2 afferents are well-characterized by specific expres-  
327 sion of two different *Mrgpr* members: NP1 neurons (~20% of total DRG neurons) highly express  
328 *Mrgprd*<sup>44</sup>, while NP2 neurons (~5% of total DRG neurons) express *Mrgpra3*<sup>15</sup>. In humans, how-  
329 ever, *MRGPRD* was only expressed in a few NP1 neurons (Fig. S9A), so it was less useful for  
330 marking human NP1 population, and *MRGPR3* gene does not have an orthologue in the human  
331 genome. In short, NP1 and NP2 populations likely have conserved physiological functions in  
332 mediating itch sensation in both mice and humans. However, some key molecular receptors for  
333 detecting pruritogens are different between the species, which may reflect evolutionary adapta-  
334 tion to distinctive pruritogens encountered by human and mice in their living environments.

335  
336 The hPEP.SST population displayed specific expression of the neuropeptide, somatostatin (*SST*),  
337 and an enriched expression of *GFRA3*, a co-receptor of tyrosine kinase RET (Fig. 3B, S7A). We  
338 also found another neuropeptide cholecystokinin (*CCK*)<sup>45</sup> enriched in this population (Fig. S7A).  
339 The hPEP.SST cluster corresponded to mouse and macaque NP3 population (Fig. 2), which are  
340 also marked by the expression of *SST*<sup>15,16</sup>. Given the previously established role of mouse NP3  
341 neurons in itch sensation<sup>46</sup> and the high expression of itch-sensing receptors, such as *HRHI*,  
342 *IL31RA* (Fig. 3A-B), hPEP.SST afferents could also mediate itch sensation, especially under  
343 inflammatory conditions<sup>15</sup>. Neither *PIEZO1* nor *PIEZO2* (Fig. S9A) was detected in hPEP.SST  
344 neurons, indicating that these afferents might not be mechanosensitive. Indeed, some human

345 histaminergic itch-sensing fibers are insensitive to mechanical forces<sup>43</sup>. A human feature of  
346 hPEP.SST neurons was the co-expression of the peptidergic neuron marker, CGRP, which was  
347 barely detected in the corresponding mouse NP3 neurons (Fig. S9B)<sup>16,18</sup>.

348

349 The hTRPM8 population was distinguished from other cell types by the specific expression of a  
350 novel molecular marker, *STUM*, and high-level expression of *TRPM8* (Fig. 3C). Almost all  
351 *STUM*<sup>+</sup> neurons expressed *TRPM8*, which was validated by multiplex FISH (Fig. 3C). Since  
352 *TRPM8* is a receptor for cold temperature and cooling chemicals (such as menthol)<sup>47-50</sup>, the  
353 hTRPM8 population likely functions as cold- and menthol-sensing afferents. Notably, this newly  
354 identified maker gene *STUM* was not detected in mouse *TRPM8*<sup>+</sup> neurons<sup>16,33</sup>. In macaque,  
355 *STUM* was more broadly expressed in several clusters (Fig. S9C)<sup>18</sup>. Nevertheless, other molecu-  
356 lar markers, such as *FOXP2* and *GPR26*, were shared among mouse<sup>16,33</sup>, macaque<sup>18</sup>, and human  
357 TRPM8 cold-sensing neurons (Fig. S9A-C). Intriguingly, some hTRPM8 neurons also expressed  
358 a low level of heat-sensing receptor *TRPV1* (Fig. 3D), suggesting that these neurons might also  
359 be activated by heat stimuli. Consistently, human physiological recordings have identified cold-  
360 sensitive C-fibers that also respond to heat<sup>51</sup>. Thus, some of the neurons in the hTRPM8 popula-  
361 tion are likely to be polymodal cold-sensing afferents.

362

363 Two peptidergic C-fiber clusters displayed overlapping high expression of *TRPV1* and *TRPA1*  
364 (Fig. 3D), which were therefore named as hPEP.TRPV1/A1.1 and hPEP.TRPV1/A1.2. Since  
365 *TRPV1* is activated by noxious heat and capsaicin, and *TRPA1* can be activated by noxious cold  
366 and various noxious chemicals<sup>52,53</sup>, they are likely to be C-fiber peptidergic thermoreceptors and  
367 nociceptors, sensing noxious thermal and chemical stimuli and transmitting pain signals. From

368 the cross-species comparison, hPEP.TRPV1/A1.1 and hPEP.TRPV1/A1.2 were mostly similar to  
369 macaque PEP1 and mouse subclass PEP1.4/CGRP- $\epsilon$  (Fig. 2A-C). The exact functional differ-  
370 ences between these two quite similar populations are yet to be established, but it is tempting to  
371 hypothesize that hPEP.TRPV1/A1.1 innervates the skin while hPEP.TRPV1/A1.2 innervates  
372 deep tissues and visceral organs, because CGRP<sup>+</sup>/TRPV1<sup>+</sup> afferents were observed in both the  
373 human skin and deep tissues<sup>54</sup>. In contrast to the hPEP.TRPV1/A1.1 population,  
374 hPEP.TRPV1/A1.2 neurons expressed PROKR2, and higher level of PTGER3, and prostaglan-  
375 din I2 receptor (PTGIR) (Fig. S7E & S9A). These molecular markers have been found to be en-  
376 riched in mouse viscera-innervating DRG neurons<sup>55,56</sup>.

377

378

### 379 **Molecular marker expression and validation of A-fiber peptidergic nociceptors**

380 Five clusters of peptidergic A-fiber nociceptors were identified in our dataset. When compared to  
381 mouse and macaque peptidergic populations, some clusters showed the greatest divergence (Fig.  
382 2A-C), indicating that they might contain human specific sensory neuron types.

383

384 The hPEP.PIEZO<sup>h</sup> cluster was named because they expressed the highest number of *PIEZO2*  
385 transcripts among all PEP clusters (Fig. 4A), an expression level comparable to the most  
386 mechanosensitive afferents, hC.LTMR and hA $\delta$ .LTMR. The hPEP.PIEZO<sup>h</sup> neurons also ex-  
387 pressed a relatively high levels of *PIEZO1* transcripts, though the overall expression of *PIEZO1*  
388 in hDRG neurons was low (Fig. S9A). This cluster could be identified by its high expression of  
389 *PTGER3* but not *TRPA1* (Fig. 4A & 3D). No mouse DRG neuron population was highly  
390 matched for the hPEP.PIEZO<sup>h</sup> cluster. Nevertheless, the expression of a few unique marker

391 genes in this cluster could provide clues into its functions. The adrenoreceptor, *ADRA2C*, a spe-  
392 cific molecular marker found in human sensory fibers innervating blood vessels<sup>57-60</sup>, was mainly  
393 detected in this cluster (Fig. S9A). In addition, the hPEP.PIEZO<sup>h</sup> population expressed *GPR68*, a  
394 membrane receptor sensing flow and shear forces in the vascular endothelia cells<sup>61</sup> (Fig. S9A).  
395 Given the well-established functions of *PIEZO1* and *PIEZO2* in mediating neuronal sensing of  
396 blood pressure and the baroreceptor reflex<sup>62</sup> and the expression of known function of *ADRA2C*  
397 and *GPR68*, we proposed that some hPEP.PIEZO<sup>h</sup> afferents innervate blood vessels and sense  
398 the blood pressure or flow. This cluster also expressed a high level of *PTGIR* (Fig. S9A). Mouse  
399 *PTGIR*<sup>+</sup> DRG neurons innervate the bladder<sup>55</sup>, and *PIEZO2* expressed in these neurons is re-  
400 quired for sensing the bladder pressure to coordinate urination<sup>63</sup>. Thus, some hPEP.PIEZO<sup>h</sup> af-  
401 ferents might also innervate bladder and play a similar role. Take all into consideration,  
402 hPEP.PIEZO<sup>h</sup> neurons might function in sensing mechanical forces from blood vessels and in-  
403 ternal organs. Given that there was not a clear mouse DRG CGRP<sup>+</sup> population with high *PIEZO2*  
404 expression from single-cell RNA-seq datasets, we speculated that hPEP.PIEZO<sup>h</sup> neurons are  
405 either human specific or greatly expanded in humans. A fundamental difference between human  
406 and mouse is their body sizes (humans are more than 2000 times larger than mice<sup>64</sup>). This addi-  
407 tion or expansion of hPEP.PIEZO<sup>h</sup> neurons is likely to meet the challenge of mediating sensation  
408 from internal organs and blood vessels in much larger human bodies.

409

410 The hPEP.KIT cluster had the specific expression of a receptor tyrosine kinase, *KIT*, and a medi-  
411 um to low expression level of *PIEZO2* (Fig. 4B). In mouse DRG neurons, *Kit* is more broadly  
412 expressed and found in four peptidergic clusters<sup>16</sup> (Fig. S9B). Cross-species analysis suggest that  
413 this cluster mainly corresponded to the mouse PEP3/CGRP- $\eta$  and macaque PEP3 population

414 (Fig. 2A-C), which are A-fiber high threshold mechanoreceptors (HTMRs), forming circumfer-  
415 ential endings around hair follicles and mediating hair pulling pain<sup>65,66</sup>. A more recent study sug-  
416 gests that mouse CGRP- $\eta$  neurons mediates mechanosensation from the distal colon<sup>67</sup>. Thus, the  
417 hPEP.KIT cluster likely functions as a population of fast-conducting mechano-nociceptors.

418

419 The third peptidergic A-fiber cluster, hPEP.CHRNA7, featured abundant expression of *CHRNA7*  
420 but almost no expression of *PIEZO2* (Fig. 4C). Cross-species analysis revealed that this cluster  
421 corresponds to mouse PEP2/CGRP- $\zeta$  and macaque PEP2 populations (Fig. 2A-C), which are also  
422 marked by the unique expression of *CHRNA7*<sup>16,18</sup>. Interestingly, this cluster also expressed  
423 *PVALB* (Fig. 1F), a molecular marker commonly used for proprioceptors in mouse and human.  
424 Retrograde tracing from the mouse gastrocnemius muscle labeled *CHRNA7*<sup>+</sup> DRG neurons<sup>55</sup>,  
425 suggesting that hPEP.CHRNA7 may contain muscle-innervating A-fiber nociceptive sensory  
426 afferents.

427

428 hPEP.NTRK3 is a population of peptidergic A-fibers with high expression of *NTRK3* and  
429 *SI00A4* (Fig. 4D). Neurons in this cluster expressed a low level of *PIEZO2* (Fig. 4B). Finally,  
430 hPEP0 is a population of peptidergic A-fibers that expressed *CALCA* and a moderate level of  
431 *PIEZO2* but lack of other specific marker genes. Potential function of hPEP.NTRK3 and hPEP0  
432 are currently unclear. They could be some types of A-fiber mechano-nociceptor<sup>68</sup>.

433

434 **Molecular marker expression and validation of C-LTMRs, A-LTMRs and an ATF3 popu-**  
435 **lation**

436 hC.LTMR is the putative human C-tactile nerve fibers. All cross-species neuron cluster compari-  
437 son methods unequivocally identified C-LTMRs as conserved across all three species. Neverthe-  
438 less, the specific marker gene *CASQ2* for hC.LTM (Fig. 5A) is not detected in either mouse or  
439 macaque C-LTMRs<sup>15,18</sup>. Conversely, mouse C.LTMR cells are characterized by exclusive ex-  
440 pression of tyrosine hydroxylase (TH) and *SLC17A8 (VGLUT3)*<sup>15</sup> (Fig. S9B), which are barely  
441 expressed in hDRG neurons (Fig. S9A). Thus, the molecular markers to identify C.LTMRs are  
442 different between human and mouse. On the other hand, human, mouse, and macaque C.LTMRs  
443 all had conserved expression of *GFRA2*, another co-receptor of RET, and a zinc finger transcrip-  
444 tion factor *ZNF521* (Fig. S9A-C). Multiplex FISH confirmed that *CASQ2*<sup>+</sup> cells expressed high  
445 levels of *PIEZO2* (Fig. 5A). hC.LTMRs likely mediate innocuous affective touch sensation<sup>70-72</sup>.

446  
447 A-LTMRs were featured by large diameter somas and high expression of *NTRK2* and *NTRK3*  
448 (Fig. 5B-C) but a lack of expressions of *SCN10A* and *PRDM12* (Fig. 4C & 1E), two genes highly  
449 associated with human nociception<sup>30,73,74</sup>. We identified 4 clusters in this category. hA $\delta$ .LTMR  
450 was named based on its high expression level of *NTRK2* and *PIEZO2*, but low level of *NTRK3*  
451 (Fig. 5A-C), a molecular feature similar to the mouse A $\delta$ -LTMRs (Fig. S9B). *KCNVI* was en-  
452 riched in this cluster and could serve as a novel molecular marker for identifying this population  
453 in hDRG neurons (Fig. 5B). hA $\beta$ .LTMR, for tactile touch, expressed higher level of *NTRK3* but  
454 a lower level of *NTRK2* compared to hA $\delta$ .LTMRs (Fig. 5C). hPropr, for limb position sensing,  
455 expressed a high level of a proprioceptor marker *PVALB* and *REEP5* (Fig. 5D).

456  
457 We also identified a cluster named as hATF3 (Fig. 5E), which contained mainly large diameter  
458 neurons and strongly corresponded the “unknown” cluster first identified in normal male mice by

459 the Sharma RNA-seq dataset<sup>16</sup>. This cluster in both human and mouse datasets showed a very  
460 conserved molecular profile (Fig. S7A). One of the markers it expressed, *ATF3*, is a transcrip-  
461 tional factor associated with sensory afferent injury, indicating that these cells may represent  
462 neurons that are undergoing (or previously underwent) stress/damage/insult (Fig. 5E). *ATF3*<sup>+</sup>  
463 neurons also expressed high level of neuropeptide *ADCYAPI* (Fig. 5E). Since there were no  
464 medical records indicating obvious nerve injuries in our human donors, and since the mouse data  
465 came from naïve mice, we speculate that these neurons might reflect a very low level of sporadic  
466 sensory afferent injury accumulated from daily lives. On the other hand, we cannot exclude the  
467 possibility that *ATF3*<sup>+</sup> cluster represent a population of normal DRG neurons.

468

469

470 **The single-soma deep RNA-seq dataset provides novel insights into the molecular and cel-**  
471 **lular mechanisms underlying human sensation of itch and pain**

472 Given the high number of unique transcripts per neuronal soma, our dataset is uniquely powerful  
473 for molecular discovery. We identified a much higher number of membrane proteins, such as  
474 GCPRs, ion channels, chemokine receptors, as well as neuropeptides, compared to 10x Visium  
475 Spatial RNA-seq or single-nucleus RNA-seq datasets (Fig. 6A). These discoveries provided nov-  
476 el insights into understanding molecular and cellular bases of physiological recording and psy-  
477 chological experiment results regarding human itch and pain sensation.

478

479 Physiological recordings have identified at least two groups of C-fibers responding to different  
480 pruritogens. One group responds to cowhage, a plant triggering intense itch in human<sup>75</sup>, and  
481 comprises mechano-sensitive polymodal units<sup>43</sup>. The other group responds to histamine with

482 sustained discharges but is mechanically insensitive<sup>43</sup>. However, the molecular and cellular bases  
483 for these observations remain unclear. To understand these physiological properties, we analyzed  
484 the expression of histamine and cowhage receptors, and the mechanoreceptor *PIEZO2* in the  
485 three potential itch populations, hNP1, hNP2 and hPEP.SST. *PIEZO2* was highly expressed in  
486 hNP1, with low expression in hNP2 and almost no detectable expression in hPEP.SST (Fig. 5A).  
487 Protease-activated receptor *F2RL1*, the receptor mediating cowhage induced itch in humans<sup>75</sup>,  
488 was exclusively expressed in hNP1 (Fig. 6B). Thus, the hNP1 population likely contained C-  
489 fiber pruriceptive afferents sensitive to both cowhage and mechanical stimuli. For histamine re-  
490 ceptors, *HRH1* was expressed in all three itch populations, *HRH2* was expressed in hNP2 and  
491 hPEP.SST but not in hNP1, *HRH3* had low expression in hNP1 and hPEP.SST, while *HRH4* was  
492 not detected (Fig. 6B-C). Thus, hNP2 and hPEP.SST clusters are good candidates for histamine-  
493 sensitive but mechano-insensitive itch-sensing C-fibers.

494

495 When intracutaneously applied into human skin, some chemicals tend to trigger itch, such as  
496 histamine and prostaglandin E2 (PGE2), while others preferentially induce pain, such as seroto-  
497 nin and bradykinin<sup>76</sup>. To explore the potential underlying mechanisms, we examined the expres-  
498 sion of all known receptors for these chemicals in our dataset. We found that the receptors of  
499 itch-inducing chemicals are enriched in itch sensing populations. For example, histamine recep-  
500 tors *HRH1* and *HRH2*, and PGE2 receptor *PTGER2* were enriched in hNP1, hNP2 and  
501 hPEP.SST putative itch-sensing neurons (Fig. S10A1). In contrast, serotonin receptors, *HTR1B*  
502 and *HTR1F*, and bradykinin receptor *BDKRB2* were enriched in putative nociceptive populations  
503 (Fig. S10A2). The differential expression patterns of these receptors might explain the different  
504 sensory experience induced by these chemicals.

505  
506  
507  
508  
509  
510  
511  
512  
513  
514  
515  
516  
517  
518  
519  
520  
521  
522  
523  
524  
525  
526

**Utility of single-soma deep RNA-seq dataset for discovering novel drug targets and for obtaining insights into molecular targets of existing drugs**

Our deep sequencing dataset can also provide novel insights into the mechanisms of existing clinical drugs or for identifying potential novel drug targets. The expression patterns of promising drug targets, such as GPCRs, ion channels, chemokine and cytokine receptors, and neuropeptides, were analyzed (Fig. S11-S14). Here we analyzed itch-related receptors and molecules as an example. A series of itch-sensing receptors have been identified in model organisms<sup>3,46,79</sup>, but which of these targets can be translated remains to be determined. A subset of these itch receptors were indeed enriched in hNP1, hNP2 and hPEP.SST populations, such as the chloroquine receptor *MRGPRX1*, bile acid receptor *MRGPRX4*, histamine receptor *HRH1*, leukotriene receptor *CYSLTR2*, and interleukin receptors *IL31RA* and *OSMR* (Fig. 6B)<sup>16,18</sup>. However, some suspected itch receptors did not exhibit expression enrichment in human itch populations. For example, *HRH4* was reported to mediate histamine-dependent itch in mice<sup>80</sup>, but expression of *HRH4* was barely detected in human itch-sensing populations (Fig. 6C), suggesting that *HRH4* might not be directly involved in human histaminergic itch. The same was found true for *IL7R* and *TLR7*<sup>79</sup>, which were proposed to mediate non-histaminergic itch in mice (Fig. 6C). In addition to these known players, we identified other membrane receptors and signaling molecules in human itch populations (Fig. 6D), including *MRGPRX3*, *EDNRA*, *PTGDR*, *HTR3A*, *CHRNA3*, *KCNG4*, and *PLCB3*, which could represent novel anti-itch targets.

527 Gabapentin was originally developed for treating epilepsy and more recently used in the treat-  
528 ment of neuropathic pain and chronic itch<sup>81</sup>. It inhibits neurotransmitter release by acting on  $\alpha\delta$ -  
529 1 and  $\alpha\delta$ -2 voltage-dependent calcium channels *CACNA2D1* and *CACNA2D2*<sup>81</sup>. We found that  
530 both receptors were broadly expressed in hDRG neurons (Fig. S10B), suggesting that one poten-  
531 tial mechanism by which gabapentin could provide clinical benefit is through inhibiting synaptic  
532 transmission of primary afferents, as has been shown in mice<sup>82</sup>.

533  
534 Opioids and derivatives activate opioid receptors to modulate pain and itch. Agonists of the  $\mu$ -  
535 opioid receptor (*OPRM1*) alleviate pain but elicit itch in humans and model organisms, whereas  
536 agonists of the  $\kappa$ -opioid receptor (*OPRK1*) inhibit itch in humans<sup>83,84</sup>. Unlike mouse DRG neu-  
537 rons, which did not display cell-type enriched expression patterns of opioid receptors (Fig.  
538 S10C), we found that opioid receptors in hDRG neurons were present in some but not other neu-  
539 ron populations. Transcripts of  $\delta$ -opioid receptor (*OPRD1*) were preferentially expressed in itch  
540 populations hNP1 and hNP2, while *OPRM1* was enriched in all hPEP clusters (Fig. S10C). Since  
541 opioid receptors are inhibitory GPCRs, our results suggest that activation of *OPRM1* could di-  
542 rectly inhibit human nociceptive afferents, while *OPRD1* could be a molecular target for inhibit-  
543 ing itch transmission. On the other hand, *OPRK1* was barely detected in our dataset, suggesting  
544 that *OPRK1* agonists may relieve itch through indirect or central mechanisms (Fig. S10C).

545

546

547 **Immunostaining of sensory fibers in the human skin using molecular markers identified by**  
548 **single-soma deep RNA-seq dataset**

549 Although human peripheral sensory afferents can be identified and visualized using the pan neu-  
550 ronal marker antibody against PGP9.5, different types of human sensory afferents cannot be dis-  
551 tinguished due to a lack of specific molecular markers. Developing an antibody panel to label  
552 different types of human sensory afferents would be invaluable for basic research, translational  
553 studies, and diagnostics. To start this direction and to test whether some molecular markers iden-  
554 tified by the single-soma RNA-seq are useful for labeling specific types of human sensory fibers,  
555 we conducted immunostaining of sensory afferents with leg skin biopsies from three normal  
556 adult donors (see Methods for detailed donor information).

557  
558 *SST* is specifically expressed in hPEP.SST neurons (Fig. 3B). Consistent with this molecular  
559 prediction, we found  $SST^+$  sensory fibers in the human skin sections in the dermis, the epider-  
560 mis-dermis junction, entering the epidermis (Fig. S15A-C), and near the hair follicle (Fig. S15D-  
561 F). In addition, double immunostaining revealed that  $SST^+$  sensory fibers were  $CGRP^+$  and made  
562 up a subset of  $CGPR^+$  sensory fibers (Fig. S15A-F). These results confirmed that human  $SST^+$   
563 sensory afferents had CGRP proteins and belonged to the PEP but not NP afferents. Since CGRP  
564 involves in neuro-immune interactions and other physiological functions<sup>85</sup>, addition of this neu-  
565 ropeptide in human  $SST^+$  afferents suggests a potential gain of new functions during evolution.

566  
567 hPEP.KIT neurons specifically express *KIT* transcripts. Strong KIT signals were observed in  
568 continuous regenerative cells at the basal layers of the skin, sweat ducts, and hair follicles, serv-  
569 ing as a positive control. A few  $KIT^+$  and  $PGP9.5^+$  sensory fibers were observed around hair fol-  
570 licles (Fig. S15G-I). Consistent with our RNA-seq results,  $KIT^+$  sensory fibers were also positive  
571 for CGRP and NEFH (Fig. S15J-O), suggesting that they were peptidergic A fibers. In short,

572 these results support that our high-fidelity hDRG neuron single-soma transcriptome dataset is  
573 useful for selecting specific molecular markers to label and visualize different types of peripheral  
574 somatosensory afferents.

575

576

577 **A novel strategy to study functions of human somatosensory afferents using single-soma**  
578 **deep RNA-seq dataset-informed microneurography recordings**

579 Molecules profiles and physiological properties of hDRG neurons are intrinsically linked: the  
580 expressed molecules form the physical basis for physiological properties. Physiological record-  
581 ings of human somatosensory afferents have been conducted for more than half a century, which  
582 generated important parts of our knowledge on the human somatosensory system. Physiological  
583 properties of somatosensory afferents generate an important foundation for informing molecular  
584 cloning of critical receptors, such as TRPV1 and PIEZO2. Due to a lack of clear molecular com-  
585 positions of human somatosensory afferents, the reverse experimental direction, from molecular  
586 profiles of human sensory afferents to inform physiological recordings, has not been possible.  
587 With the single-soma deep RNA-seq dataset, we were finally in a position to do so. Here we fo-  
588 cused on two populations of human sensory afferents to demonstrate the feasibility and power of  
589 using single-soma deep RNA-seq informed microneurography recordings to study the function  
590 of human afferent subtypes.

591

592 As mentioned previously, the hPEP.KIT population was highly correlated to the mouse  
593 PEP3/CGRP- $\eta$  cluster<sup>15,18</sup> (Fig. 2A-C), a population of TRPV1-negative A-fiber fast-conducting  
594 hair pull-sensitive mechano-nociceptors<sup>86</sup>. Our single-soma deep RNA-seq data revealed that

595 hPEP.KIT neurons express NEFH and PIEZO2, but not TRPV1 (Fig. 7A), suggesting that they  
596 were A-fiber mechano-nociceptors without heat/capsaicin sensitivity. Interestingly, our dataset  
597 also revealed that hPEP.KIT neurons expressed a low level of *TRPM8* (Fig. 7A), a feature that  
598 has not been reported in mice. Multiplex FISH validated the co-expression of *KIT*, *PIEZO2* and  
599 *TRPM8* in hDRG neurons (Fig. S16A). Altogether, these molecular profiles suggest that  
600 hPEP.KIT neurons may be A-fiber HTMRs, responsive to cooling but not heating. Thus, we hy-  
601 pothesized that there exist some previously uncharacterized fast-conducting A-fiber HTMRs in  
602 the human skin, which can be activated by cooling but not heating stimuli.

603

604 To test this idea, using the *in vivo* electrophysiological technique of microneurography, single-  
605 unit axonal recordings were performed from the radial, antebrachial, and peroneal nerves of  
606 healthy participants (Fig. 7B-D). The A-HTMRs (n=10) were identified by their insensitivity to  
607 soft-brush stroking while responding to a rough brush and displaying high indentation thresholds  
608 ( $\geq 4$  mN); further, they had A $\beta$ -range conduction velocities ( $>30$  m/s, Fig. 7B-F). Remarkably, a  
609 subtype of these heat-insensitive A-HTMRs (n=5) units responded to cooling (Fig. 7G-H). Com-  
610 pared to mechanically evoked responses, those evoked by cooling although relatively modest but  
611 reproducible with tested in triplicates for each recording (Fig. S16B). Furthermore, these cool-  
612 ing-evoked responses persisted during the sustained phase (Fig. S16B). These observations con-  
613 firmed our prediction that some human cutaneous A-HTMRs are cold-sensitive but heat-  
614 insensitive. Based on the transcriptome dataset and current knowledge about molecular receptors  
615 for heat and cold, hPEP.KIT seems to be the only population that has the molecular basis for this  
616 distinct combination of physiological properties. Thus, we propose that the molecularly defined

617 hPEP.KIT population is correlated to the physiologically defined A-HTMRs with cold but not  
618 heat sensitivity (Fig. 7I).

619

620 Human C-LTMRs are readily found during microneurography recordings from the upper limb  
621 including the distal regions<sup>87</sup>, but they seem to sparsely innervate the distal lower limb<sup>88</sup>. This is  
622 consistent with our sequencing results wherein the hC.LTMRs constituted a small population of  
623 neurons in lower thoracic and lumbar level DRGs (Fig. 1G). Unexpectedly, our sequencing data  
624 revealed that human hC.LTMRs had almost no expression of the cold and menthol receptor  
625 *TRPM8* (Fig. 8A) though C.LTMRs display sensitivity to cooling in both humans and mice<sup>89,90</sup>.  
626 Another unexpected finding was that hC.LTMRs expressed *TRPV1* (Fig. 8A). Multiplex FISH  
627 confirmed that *CASQ2*<sup>+</sup> hC.LTMRs were *TRPM8*<sup>-</sup> but *TRPV1*<sup>+</sup> (Fig. S17A). This expression  
628 pattern suggested that hC.LTMRs might respond to heating and capsaicin, a novel physiological  
629 property that has not been discovered in rodent or non-human primate models, but is predicted  
630 not to respond to menthol. In human microneurography, the C-LTMRs (n=11) were identified by  
631 their soft-brush sensitivity, low indentation threshold (in this case,  $\leq 0.7$  mN), and slow conduc-  
632 tion velocity ( $\sim 1$  m/s, n=11, Fig. 7B-C, 8B-D). Consistent with mouse C-LTMRs, these human  
633 counterparts responded to hair movement (Fig. 8D) and dynamic cooling (Fig. 8E). In two of  
634 them, after having confirmed the cooling response, we applied menthol to their individual recep-  
635 tive fields resulting in a cold sensation, but the recorded C-LTMRs, while still responsive to me-  
636 chanical and thermal stimuli, were not activated by menthol (Fig. 8F). Remarkably,  
637 microneurography recordings showed that a subset of human C-LTMRs responded to dynamic  
638 heating (5 out of 11 units or 45%, example shown in Fig. 8G). This proportion of heat-sensitive  
639 C-LTMRs aligns with findings in the rabbit (8 out of 18 units or 44%)<sup>91</sup>. In three C-LTMRs,

640 after having confirmed the heating response, we applied capsaicin to their receptive fields. Con-  
641 sistent with the sequencing results, all three were activated by capsaicin (Fig. 8H). Relative to  
642 mechanical stimulation, the C-LTMR responses to dynamic temperature changes were compara-  
643 tively modest. However, these responses were reproducible, having been tested in triplicates for  
644 each modality and recording (Fig. S16B-C). Interestingly, the C-LTMR has different cooling  
645 response properties compared to A-HTMR cooling+ fibers. The cooling-evoked responses rapid-  
646 ly diminished in C-TLMR but persisted during the sustained phase in A-HTMR cooling+ fibers.  
647 The existence of a polymodal (mechano-heat-cold) C-LTMR type is novel and confirms the se-  
648 quencing predictions. Furthermore, the cooling response must be mediated through a non-  
649 TRPM8 mechanism.

650

651 For comparison, our recordings also identified C-HTMRs (n=11) that did not respond to soft-  
652 brush stroking and hair movement (they responded to a rough brush), had high indentation  
653 thresholds (in this case,  $\geq 10$  mN), and slow conduction velocities ( $\sim 1$  m/s, Fig. 7B-D & S17B-E).  
654 Based on their temperature responses (tested in 9 units), a mix of C-fiber mechano-heat (n=6), C-  
655 fiber mechano-cold (n=2), and C-fiber polymodal (mechano-heat-cold, n=1) subtypes were iden-  
656 tified. An example of heating and capsaicin responses of a C-fiber mechano-heat nociceptor is  
657 shown in Fig. S17F-G. Collectively, these results highlight the accuracy and utility of our single-  
658 soma deep RNA-seq dataset of hDRG neurons in guiding and informing the functional character-  
659 ization of human somatosensory afferents and the power of combining the two approaches. We  
660 believe that this signifies a promising new research direction to link molecular and physiological  
661 types and to discover novel functional properties of human somatosensory afferents.

662

663

## 664 **Discussion**

665 Despite the high relevance to human health, molecular and cellular mechanisms underlying nor-  
666 mal and pathological human somatosensation remain largely elusive. In this study, we developed  
667 a novel LCM-based approach for single-soma deep RNA-seq and recovered more than 9000  
668 unique transcripts per neuron over 1000 adult hDRG neurons. The sequenced hDRG neurons  
669 were clustered into 16 molecular groups, displaying similarities to and remarkable differences  
670 from macaque and mouse DRG neurons. As exemplified in the study, our dataset provides im-  
671 portant and novel insights into human pain and itch sensory phenomena, explains mechanisms of  
672 drug effects, and represents a rich resource to identify new molecular targets for modulating the  
673 activity of itch- and pain-sensing primary afferents. Moreover, our dataset successfully guided  
674 histological labeling (Fig. S15) and physiological recording (Fig. 7, 8 & S17) of different types  
675 of human sensory afferents, leading to discovery of their new anatomical features and physiolog-  
676 ical properties, and serving as a common ground to connect them all together (Fig. 7I).

677

678 Single-cell RNA-seq of human DRG/TG neurons has been technically challenging. One main  
679 hurdle is to isolate sensory neurons from a large population of non-neuronal cells. The traditional  
680 enzymatic and mechanical dissociation method is incompatible with human DRG/TG neurons.  
681 Strategies, including spatial transcriptomics and single-nucleus RNA-seq<sup>22,23,92</sup>, have generated  
682 some pioneering datasets characterizing the molecular profiles of human DRG and TG neurons.  
683 Nevertheless, the number of transcripts, sequencing depth, or single-cell resolution of the previ-  
684 ous studies needs to be improved. Importantly, though nuclear and soma transcripts are intrinsi-  
685 cally linked and overlapping to some extent, the soma contains much more transcripts both quan-

686 titatively and qualitatively. Soma transcripts are also one step closer than nuclear transcripts for  
687 functions. Thus, soma transcripts are preferable, if available, for cell type clustering and func-  
688 tional interpretation. In this study, we developed a new strategy by combining fresh frozen  
689 hDRG tissues, cryo-section, laser capture microdissection of individual neuronal soma, and  
690 Smart-seq2 deep sequencing. Fresh frozen tissue and cryosection techniques minimized  
691 transcriptomic changes during the tissue transportation and single-cell isolation process. LCM  
692 allowed isolation of DRG neuronal soma with minimal contamination from surrounding non-  
693 neuronal cells, while preserving information about cellular morphology, and the Smart-seq2 pro-  
694 tocol enabled a high recovery rate of mRNA molecules. Although LCM has been used for isolat-  
695 ing a group of neurons for RNA-seq<sup>6,7</sup> or single TG neurons for genomic DNA analysis<sup>93</sup>, the  
696 successful application of LCM for single-cell transcriptomic analysis has not been achieved be-  
697 fore. Thus, we have established a new method for single-cell RNA-seq of adult hDRG neurons.  
698 Our approach should be readily applicable to other human neurons with large soma sizes, such as  
699 other peripheral ganglia neurons, motor neurons, etc.

700

701 Different single-cell RNA-seq approaches, including single-nucleus RNA-seq<sup>21,23,92</sup>, spatial  
702 transcriptomics<sup>22</sup>, and our LCM-based single-soma RNA-seq, have generated four datasets of  
703 transcriptome profiles and cell type clusters of hDRG neurons. These datasets and results overlap  
704 to some extent but also exhibit some significant differences (an example shown in Fig. S4). The  
705 observed differences are likely caused by both biological and technical features associated with  
706 each method. Given the high sequencing depth of transcripts from the neuronal soma, our ap-  
707 proach is powerful for molecular discovery, especially for functional molecules expressed at a  
708 low level. For example, our approach detected the specific expression of *MRGPRX1* and

709 *MRGPRX4*, two important pruritogen-sensing GPCRs, in hNP1 and/or hNP2 neurons, while the  
710 previous datasets barely or not detected these transcripts<sup>22,23</sup>. Our analysis of the expression of  
711 receptors, ion channels, and neuropeptides, in human itch-sensing DRG neurons have also identi-  
712 fied a set of potential new targets for modulating activities of these sensory afferents (Fig. 6).

713

714 In addition, our sequencing and microneurography results raise many interesting questions re-  
715 garding the molecular receptors and afferent types involved in human cold and mechanical pain  
716 sensation. For example, human hC.LTMRs rely on a non-TRPM8 cold receptor or another  
717 mechanism for their cooling sensitivity<sup>88</sup>. We noticed a low expression level of *TRPA1*, which  
718 also has cold sensitivity<sup>94,95</sup>, within this population (Fig. S7E). Whether *TRPA1* or some current-  
719 ly unknown cold receptors mediate cooling sensitivity in this population will be of interest for  
720 future research. The discovery of the hPEP.KIT population indicated a potential role for *PIEZO2*  
721 in human mechano-nociception. This population also responded to cooling, which is a curious  
722 property of a large-diameter myelinated nociceptor. Our discovery of TRPM8 expression in the-  
723 se neurons provides a molecular explanation for this unique property. In addition, a likely mo-  
724 lecular type for C-HTMRs, which display a mixture of responsiveness to mechanical forces and  
725 temperature, is the hPEP.TRPV1/A1.1 population. Since hPEP.TRPV1/A1.1 neurons have no  
726 expression of *PIEZO2* or *PIEZO1* (Fig. S9A), a non-*PIEZO* mechanoreceptor may exist in these  
727 neurons for mediating mechanical pain sensation. This is consistent with reports that patients  
728 with *PIEZO2* loss-of-function mutations still have normal mechanical pain threshold and sensi-  
729 tivity<sup>68,96</sup>. One suggested mechanical pain channel, TMEM120A (TACAN), is broadly expressed  
730 in all types of hDRG neurons (Fig. S9A). This expression pattern does not support its purported  
731 role as a mechanical pain receptor in humans. Both C-LTMRs and A-HTMRs responded to cool-

732 ing in human microneurography. While the responses were comparatively modest in contrast to  
733 mechanically evoked responses, they were consistent on a trial-to-trial basis. This suggests that  
734 the requisite circuitry may already be in place, which could potentially have implications for un-  
735 derstanding thermal hypersensitivities in pathological states. Indeed, there is indirect evidence  
736 from human psychophysics and targeted pharmacology, pointing to the role of C-LTMRs in me-  
737 diating acute cold allodynia<sup>97</sup> and the role of A fibers in signaling chronic cold allodynia<sup>98</sup>. In  
738 short, our dataset serves as an important atlas for understanding sensory properties of hDRG af-  
739 ferents and somatosensation more generally.

740

741 Insights into the relationship of the neuronal types between the mouse and human are essential,  
742 as such knowledge is important for translation of pre-clinical discoveries and for inferring func-  
743 tions of human sensory afferents. The three different analysis strategies used in this study com-  
744 plement each other as they have different strength and weakness (see Methods for details). To  
745 our satisfaction, despite the different advantages and disadvantages, results from these methods  
746 were highly consistent with each other (Fig. 2 & S5). Our results suggested that many broader  
747 functional groups of DRG sensory afferents are conserved across species, despite noticeably mo-  
748 lecular differences (Fig. 2 & S6). The greatest divergence between mouse and hDRG neurons  
749 was observed among C- and A-fiber nociceptors. Mice contain four C-fiber nociceptors (PEP1  
750 neuron subtypes), two expressing TRPV1 but not TRPA1 or PIEZO2 (PEP1.1 and PEP1.2) and  
751 another two which expresses all three channels (PEP1.3 and PEP1.4) (Fig. 2A & 2C). While not  
752 much is known about mouse PEP1.2/CGRP beta, PEP1.1 represents a noxious heat sensory type,  
753 terminating with free nerve endings in epidermis of hairy skin<sup>99</sup>. PEP1.3/CGRP gamma neurons  
754 innervate mainly internal organs and are a silent nociceptor type, becoming active during in-

755 inflammation<sup>100</sup>. No functional studies have been performed on PEP1.4 in the mouse. These neu-  
756 rons are speculated to represent C-HTMRs which are functionally known to exist in the mouse<sup>101</sup>.  
757 In humans, it seems that this diversity of C-fiber nociceptors has conflated into two types, the  
758 hPEP.TRPV1/A1.1 and hPEP.TRPV1/A1.2 (Fig. 2A & 2C), expressing both TRPV1/TRPA1  
759 with or without PIEZO2, respectively. If similar to mice, different neuronal populations in hu-  
760 man are somewhat specialized according localization of peripheral target, one of these types may  
761 represent deeply innervating silent nociceptors, known to be present in human<sup>102</sup>, and the other  
762 involved in slow noxious thermal and burning cutaneous sensation and perhaps joint pain. One  
763 thing to note is that our dataset contains transcriptomes of hDRG neurons from the lower thorac-  
764 ic and lumbar levels, which mainly convey sensations from the leg and lower back. Thus, it re-  
765 mains an open question whether humans have a population of internal organ-specific C-  
766 nociceptors, like the mouse PEP1.3 cluster. This question will be resolved when sequencing  
767 more hDRG neurons from the thoracic level.

768

769 For A-fiber nociceptors, only two types have been identified in mice. The PEP2/CGRP-zeta  
770 mechano-heat nociceptive population expresses PIEZO2 and low levels of TRPV1<sup>16,33</sup>, con-  
771 sistent with heat activation only at very high temperatures<sup>99</sup>, and the PEP3/CGRP-eta mechano-  
772 nociceptive conveying fast and sharp pain, including hair pulling<sup>44,103</sup>. In this study, we identified  
773 five types A-fiber nociceptors in hDRG neurons (Fig. 1G, 2A & 2C). Two populations have  
774 clearly conserved features to mouse: hPEP.CHRNA7 showed molecular similarities to mouse  
775 and macaque PEP2/CGRP-ζ, and hPEP.KIT to mouse and macaque PEP3/CGRP-η. The other  
776 three populations displayed much greater divergence (i.e. hPEP.NTRK3, hPEP.PIEZO<sup>h</sup>, and  
777 hPEP.0). The hPEP.PIEZO<sup>h</sup> cluster is particularly interesting since these neurons express very

778 high levels of *PIEZO2* and *PIEZO1*, unlike any neuron types in the mouse. Our results suggest  
779 that fast pain and interoception might have been an evolutionary preference in humans as com-  
780 pared to rodents, an effect that may relate to significantly increased human body sizes.

781

782 Finally, in this study, we sequenced over 1000 DRG neurons from 6 DRGs at the thoracic (T11-  
783 T12) and lumbar (L2-L5) levels of three Caucasian human donors with no obvious somatosensory  
784 or systematic diseases and substance uses (Supplementary tables 1 & 2). It is about ~150 to  
785 200 neurons per DRG, which represent 1-2% of the total neurons within a hDRG. Thus, sequenc-  
786 ing more neurons might give an improved representation. The existence of different types of RA  
787 and SA A $\beta$ -LTMRs and different types of proprioceptors in humans is well known, but our cur-  
788 rent dataset did not have the resolution yet to separate them (Fig. 1G). With increased number of  
789 neurons sequenced, we anticipate discovering an even greater heterogeneity among hDRG neu-  
790 rons. In addition, DRGs at different spinal levels innervate different peripheral target tissues<sup>29</sup>.  
791 Sequencing DRG neurons from different spinal levels will help to uncover molecular and cellu-  
792 lar mechanisms underlying physiological functions. Moreover, increased sampling from addi-  
793 tional donors representing different demographics would also be critical for investigating sex,  
794 race, and age-related differences. Last but not the least, pathological conditions greatly alter the  
795 transcriptomic landscape<sup>104,105</sup>. Systematic comparison of molecular and cellular changes be-  
796 tween donors at the baseline condition (like the screening criteria of this study) and those with  
797 chronic itch or chronic pain would be of great value, if samples are available, for understanding  
798 pathological mechanisms and for identifying molecular targets for effective treatments.

799

800

801  
802  
803  
804  
805  
806  
807  
808  
809  
810  
811  
812  
813  
814  
815  
816  
817  
818  
819  
820  
821  
822  
823

**Reference:**

- 1 Nascimento, A. I., Mar, F. M. & Sousa, M. M. The intriguing nature of dorsal root ganglion neurons: Linking structure with polarity and function. *Prog Neurobiol* **168**, 86-103, doi:10.1016/j.pneurobio.2018.05.002 (2018).
- 2 Purves, D. A., George J.; Fitzpatrick, David; Katz, Lawrence C.; LaMantia, Anthony-Samuel; McNamara, James O.; Williams, S. Mark. The Major Afferent Pathway for Mechanosensory Information: The Dorsal Column-Medial Lemniscus System. *Neuroscience. 2nd edition* (2001).
- 3 Azimi, E., Xia, J. & Lerner, E. A. Peripheral mechanisms of itch. *Itch-Management in Clinical Practice* **50**, 18-23 (2016).
- 4 Mills, S. E. E., Nicolson, K. P. & Smith, B. H. Chronic pain: a review of its epidemiology and associated factors in population-based studies. *Br J Anaesth* **123**, e273-e283, doi:10.1016/j.bja.2019.03.023 (2019).

- 824 5 Manglik, A. *et al.* Structure-based discovery of opioid analgesics with reduced side  
825 effects. *Nature* **537**, 185-190, doi:10.1038/nature19112 (2016).
- 826 6 Yosipovitch, G., Rosen, J. D. & Hashimoto, T. Itch: From mechanism to (novel)  
827 therapeutic approaches. *J Allergy Clin Immunol* **142**, 1375-1390,  
828 doi:10.1016/j.jaci.2018.09.005 (2018).
- 829 7 Burma, N. E., Leduc-Pessah, H., Fan, C. Y. & Trang, T. Animal models of chronic pain:  
830 advances and challenges for clinical translation. *Journal of neuroscience research* **95**,  
831 1242-1256 (2017).
- 832 8 Hill, R. NK1 (substance P) receptor antagonists—why are they not analgesic in humans?  
833 *Trends in pharmacological sciences* **21**, 244-246 (2000).
- 834 9 Haberberger, R. V., Barry, C., Dominguez, N. & Matusica, D. Human Dorsal Root  
835 Ganglia. *Front Cell Neurosci* **13**, 271, doi:10.3389/fncel.2019.00271 (2019).
- 836 10 Middleton, S. J. *et al.* Studying human nociceptors: from fundamentals to clinic. *Brain*  
837 **144**, 1312-1335 (2021).
- 838 11 Yu, H. *et al.* MRGPRX4 is a bile acid receptor for human cholestatic itch. *Elife* **8**, e48431  
839 (2019).
- 840 12 Alemi, F. *et al.* The TGR5 receptor mediates bile acid-induced itch and analgesia. *The*  
841 *Journal of clinical investigation* **123**, 1513-1530 (2013).
- 842 13 Tang, F. *et al.* mRNA-Seq whole-transcriptome analysis of a single cell. *Nat Methods* **6**,  
843 377-382, doi:10.1038/nmeth.1315 (2009).
- 844 14 Hwang, B., Lee, J. H. & Bang, D. Single-cell RNA sequencing technologies and  
845 bioinformatics pipelines. *Exp Mol Med* **50**, 96, doi:10.1038/s12276-018-0071-8 (2018).
- 846 15 Usoskin, D. *et al.* Unbiased classification of sensory neuron types by large-scale single-

- 847 cell RNA sequencing. *Nature neuroscience* **18**, 145-153 (2015).
- 848 16 Sharma, N. *et al.* The emergence of transcriptional identity in somatosensory neurons.  
849 *Nature* **577**, 392-398 (2020).
- 850 17 Wang, K. *et al.* Single-cell transcriptomic analysis of somatosensory neurons uncovers  
851 temporal development of neuropathic pain. *Cell research* **31**, 904-918 (2021).
- 852 18 Kupari, J. *et al.* Single cell transcriptomics of primate sensory neurons identifies cell  
853 types associated with chronic pain. *Nature communications* **12**, 1-15 (2021).
- 854 19 Stuart, T. *et al.* Comprehensive integration of single-cell data. *Cell* **177**, 1888-1902.  
855 e1821 (2019).
- 856 20 Mattei, D. *et al.* Enzymatic dissociation induces transcriptional and proteotype bias in  
857 brain cell populations. *International journal of molecular sciences* **21**, 7944 (2020).
- 858 21 Jung, M. *et al.* Cross-species transcriptomic atlas of dorsal root ganglia reveals species-  
859 specific programs for sensory function. *Nature Communications* **14**, 366 (2023).
- 860 22 Tavares-Ferreira, D. *et al.* Spatial transcriptomics of dorsal root ganglia identifies  
861 molecular signatures of human nociceptors. *Science translational medicine* **14**, eabj8186  
862 (2022).
- 863 23 Nguyen, M. Q., von Buchholtz, L. J., Reker, A. N., Ryba, N. J. & Davidson, S. Single-  
864 nucleus transcriptomic analysis of human dorsal root ganglion neurons. *Elife* **10**, e71752  
865 (2021).
- 866 24 Bhuiyan, S. *et al.* Harmonized cross-species cell atlases of trigeminal and dorsal root  
867 ganglia. *bioRxiv*, 2023.2007.2004.547740 (2023).
- 868 25 Ding, J. *et al.* Systematic comparison of single-cell and single-nucleus RNA-sequencing  
869 methods. *Nature biotechnology* **38**, 737-746 (2020).

- 870 26 Picelli, S. *et al.* Full-length RNA-seq from single cells using Smart-seq2. *Nature*  
871 *protocols* **9**, 171-181 (2014).
- 872 27 Hao, Y. *et al.* Integrated analysis of multimodal single-cell data. *Cell* **184**, 3573-3587.  
873 e3529 (2021).
- 874 28 Abraira, V. E. & Ginty, D. D. The sensory neurons of touch. *Neuron* **79**, 618-639,  
875 doi:10.1016/j.neuron.2013.07.051 (2013).
- 876 29 Luo, L. *PRINCIPLES OF NEUROBIOLOGY*. 265-267 (Garland Science, 2016).
- 877 30 Chen, Y.-C. *et al.* Transcriptional regulator PRDM12 is essential for human pain  
878 perception. *Nature genetics* **47**, 803-808 (2015).
- 879 31 Barkas, N. *et al.* Joint analysis of heterogeneous single-cell RNA-seq dataset collections.  
880 *Nature methods* **16**, 695-698 (2019).
- 881 32 Jovic, D. *et al.* Single-cell RNA sequencing technologies and applications: A brief  
882 overview. *Clin Transl Med* **12**, e694, doi:10.1002/ctm2.694 (2022).
- 883 33 Zeisel, A. *et al.* Molecular architecture of the mouse nervous system. *Cell* **174**, 999-1014.  
884 e1022 (2018).
- 885 34 Hippenmeyer, S. *et al.* A developmental switch in the response of DRG neurons to ETS  
886 transcription factor signaling. *PLoS biology* **3**, e159 (2005).
- 887 35 Jeub, M. *et al.* The transcription factor Smad-interacting protein 1 controls pain  
888 sensitivity via modulation of DRG neuron excitability. *PAIN®* **152**, 2384-2398 (2011).
- 889 36 Scott, A. *et al.* Transcription factor short stature homeobox 2 is required for proper  
890 development of tropomyosin-related kinase B-expressing mechanosensory neurons.  
891 *Journal of Neuroscience* **31**, 6741-6749 (2011).
- 892 37 Abdo, H. *et al.* Dependence on the transcription factor Shox2 for specification of sensory

- 893 neurons conveying discriminative touch. *European Journal of Neuroscience* **34**, 1529-  
894 1541 (2011).
- 895 38 Levanon, D. *et al.* The Runx3 transcription factor regulates development and survival of  
896 TrkC dorsal root ganglia neurons. *The EMBO journal* **21**, 3454-3463 (2002).
- 897 39 Chen, C.-L. *et al.* Runx1 determines nociceptive sensory neuron phenotype and is  
898 required for thermal and neuropathic pain. *Neuron* **49**, 365-377 (2006).
- 899 40 Vermeiren, S., Bellefroid, E. J. & Desiderio, S. Vertebrate sensory ganglia: common and  
900 divergent features of the transcriptional programs generating their functional  
901 specialization. *Frontiers in Cell and Developmental Biology* **8**, 587699 (2020).
- 902 41 Liu, Q. & Dong, X. The role of the Mrgpr receptor family in itch. *Pharmacology of itch*,  
903 71-88 (2015).
- 904 42 Meixiong, J., Vasavda, C., Snyder, S. H. & Dong, X. MRGPRX4 is a G protein-coupled  
905 receptor activated by bile acids that may contribute to cholestatic pruritus. *Proc Natl*  
906 *Acad Sci U S A* **116**, 10525-10530, doi:10.1073/pnas.1903316116 (2019).
- 907 43 Namer, B. *et al.* Separate peripheral pathways for pruritus in man. *Journal of*  
908 *neurophysiology* **100**, 2062-2069 (2008).
- 909 44 Dong, P. *et al.* TRPC3 is dispensable for  $\beta$ -alanine triggered acute itch. *Scientific reports*  
910 **7**, 1-12 (2017).
- 911 45 Rehfeld, J. F. Cholecystokinin and the hormone concept. *Endocrine Connections* **10**,  
912 R139-R150 (2021).
- 913 46 McNeil, B. & Dong, X. Peripheral mechanisms of itch. *Neuroscience bulletin* **28**, 100-  
914 110 (2012).
- 915 47 Colburn, R. W. *et al.* Attenuated cold sensitivity in TRPM8 null mice. *Neuron* **54**, 379-

- 916 386 (2007).
- 917 48 Bautista, D. M. *et al.* The menthol receptor TRPM8 is the principal detector of  
918 environmental cold. *Nature* **448**, 204-208 (2007).
- 919 49 Dhaka, A. *et al.* TRPM8 is required for cold sensation in mice. *Neuron* **54**, 371-378  
920 (2007).
- 921 50 Samour, M. S., Nagi, S. S. & Mahns, D. A. Cav3. 2-expressing low-threshold C fibres in  
922 human hairy skin contribute to cold allodynia—a non-TRPV1-and non-TRPM8-  
923 dependent phenomenon. *Pain* **156**, 1566-1575 (2015).
- 924 51 Campero, M., Baumann, T., Bostock, H. & Ochoa, J. Human cutaneous C fibres  
925 activated by cooling, heating and menthol. *The Journal of physiology* **587**, 5633-5652  
926 (2009).
- 927 52 Caterina, M. J. *et al.* The capsaicin receptor: a heat-activated ion channel in the pain  
928 pathway. *Nature* **389**, 816-824 (1997).
- 929 53 Bandell, M. *et al.* Noxious cold ion channel TRPA1 is activated by pungent compounds  
930 and bradykinin. *Neuron* **41**, 849-857 (2004).
- 931 54 Defaye, M. *et al.* Gut-innervating TRPV1+ neurons drive chronic visceral pain via  
932 microglial P2Y12 receptor. *Cellular and Molecular Gastroenterology and Hepatology*  
933 **13**, 977-999 (2022).
- 934 55 Yang, F.-C. *et al.* Genetic control of the segregation of pain-related sensory neurons  
935 innervating the cutaneous versus deep tissues. *Cell reports* **5**, 1353-1364 (2013).
- 936 56 Liu, S. *et al.* A neuroanatomical basis for electroacupuncture to drive the vagal–adrenal  
937 axis. *Nature* **598**, 641-645 (2021).
- 938 57 Albrecht, P. J. *et al.* Pathologic alterations of cutaneous innervation and vasculature in

939 affected limbs from patients with complex regional pain syndrome. *Pain* **120**, 244-266  
940 (2006).

941 58 Morelli, C. *et al.* Identification of a population of peripheral sensory neurons that  
942 regulates blood pressure. *Cell reports* **35**, 109191 (2021).

943 59 Albrecht, P. J. *et al.* Excessive peptidergic sensory innervation of cutaneous arteriole–  
944 venule shunts (AVS) in the palmar glabrous skin of fibromyalgia patients: Implications  
945 for widespread deep tissue pain and fatigue. *Pain medicine* **14**, 895-915 (2013).

946 60 Bowsher, D. *et al.* Absence of pain with hyperhidrosis: a new syndrome where vascular  
947 afferents may mediate cutaneous sensation. *PAIN®* **147**, 287-298 (2009).

948 61 Xu, J. *et al.* GPR68 senses flow and is essential for vascular physiology. *Cell* **173**, 762-  
949 775. e716 (2018).

950 62 Zeng, W.-Z. *et al.* PIEZOs mediate neuronal sensing of blood pressure and the  
951 baroreceptor reflex. *Science* **362**, 464-467 (2018).

952 63 Marshall, K. L. *et al.* PIEZO2 in sensory neurons and urothelial cells coordinates  
953 urination. *Nature* **588**, 290-295 (2020).

954 64 Perlman, R. L. Mouse models of human disease: an evolutionary perspective. *Evolution,*  
955 *medicine, and public health* **2016**, 170-176 (2016).

956 65 Willimann, B. & Trüeb, R. M. Hair pain (trichodynia): frequency and relationship to hair  
957 loss and patient gender. *Dermatology* **205**, 374-377 (2002).

958 66 von Buchholtz, L. J. *et al.* Decoding cellular mechanisms for mechanosensory  
959 discrimination. *Neuron* **109**, 285-298. e285 (2021).

960 67 Wolfson, R. L. *et al.* DRG afferents that mediate physiologic and pathologic  
961 mechanosensation from the distal colon. *Cell* **186**, 3368–3385 (2023).

- 962 68 Nagi, S. S. *et al.* An ultrafast system for signaling mechanical pain in human skin.  
963 *Science advances* **5**, eaaw1297 (2019).
- 964 69 Schmidt, R. F. *Encyclopedia of Pain*. pp 2171–2173 (Springer 2007).
- 965 70 Löken, L. S., Wessberg, J., McGlone, F. & Olausson, H. Coding of pleasant touch by  
966 unmyelinated afferents in humans. *Nature neuroscience* **12**, 547-548 (2009).
- 967 71 Olausson, H., Wessberg, J., McGlone, F. & Vallbo, Å. The neurophysiology of  
968 unmyelinated tactile afferents. *Neuroscience & Biobehavioral Reviews* **34**, 185-191  
969 (2010).
- 970 72 Huzard, D. *et al.* The impact of C-tactile low-threshold mechanoreceptors on affective  
971 touch and social interactions in mice. *Science Advances* **8**, eabo7566 (2022).
- 972 73 Xue, Y., Chidiac, C., Herault, Y. & Gaveriaux-Ruff, C. Pain behavior in SCN9A (Nav1.  
973 7) and SCN10A (Nav1. 8) mutant rodent models. *Neuroscience Letters* **753**, 135844  
974 (2021).
- 975 74 Duan, G. *et al.* A SCN10A SNP biases human pain sensitivity. *Molecular pain* **12**,  
976 1744806916666083 (2016).
- 977 75 Reddy, V. B., Iuga, A. O., Shimada, S. G., LaMotte, R. H. & Lerner, E. A. Cowhage-  
978 evoked itch is mediated by a novel cysteine protease: a ligand of protease-activated  
979 receptors. *Journal of Neuroscience* **28**, 4331-4335 (2008).
- 980 76 Schmelz, M. *et al.* Chemical response pattern of different classes of C-nociceptors to  
981 pruritogens and algogens. *Journal of neurophysiology* **89**, 2441-2448 (2003).
- 982 77 Dahlhamer, J. *et al.* Prevalence of Chronic Pain and High-Impact Chronic Pain Among  
983 Adults - United States, 2016. *MMWR Morb Mortal Wkly Rep* **67**, 1001-1006,  
984 doi:10.15585/mmwr.mm6736a2 (2018).

- 985 78 Tajiri, K. & Shimizu, Y. Recent advances in the management of pruritus in chronic liver  
986 diseases. *World J Gastroenterol* **23**, 3418-3426, doi:10.3748/wjg.v23.i19.3418 (2017).
- 987 79 Dong, X. & Dong, X. Peripheral and central mechanisms of itch. *Neuron* **98**, 482-494  
988 (2018).
- 989 80 Bell, J., McQueen, D. & Rees, J. Involvement of histamine H4 and H1 receptors in  
990 scratching induced by histamine receptor agonists in BalbC mice. *British journal of*  
991 *pharmacology* **142**, 374-380 (2004).
- 992 81 Calandre, E. P., Rico-Villademoros, F. & Slim, M. Alpha2delta ligands, gabapentin,  
993 pregabalin and mirogabalin: a review of their clinical pharmacology and therapeutic use.  
994 *Expert review of neurotherapeutics* **16**, 1263-1277 (2016).
- 995 82 Peng, C. *et al.* miR-183 cluster scales mechanical pain sensitivity by regulating basal and  
996 neuropathic pain genes. *Science* **356**, 1168-1171 (2017).
- 997 83 Cowan, A., Kehner, G. B. & Inan, S. Targeting itch with ligands selective for  $\kappa$  opioid  
998 receptors. *Pharmacology of itch*, 291-314 (2015).
- 999 84 Ko, M. H., Song, M., Edwards, T., Lee, H. & Naughton, N. The role of central  $\mu$  opioid  
1000 receptors in opioid-induced itch in primates. *Journal of Pharmacology and Experimental*  
1001 *Therapeutics* **310**, 169-176 (2004).
- 1002 85 Chu, C., Artis, D. & Chiu, I. M. Neuro-immune interactions in the tissues. *Immunity* **52**,  
1003 464-474 (2020).
- 1004 86 Ghitani, N. *et al.* Specialized mechanosensory nociceptors mediating rapid responses to  
1005 hair pull. *Neuron* **95**, 944-954. e944 (2017).
- 1006 87 Xu, S. *et al.* Mechanoreceptive A $\beta$  primary afferents discriminate naturalistic social touch  
1007 inputs at a functionally relevant time scale. *bioRxiv*, 2023.2007. 2022.549516 (2023).

- 1008 88 Löken, L. S., Backlund Wasling, H., Olausson, H., McGlone, F. & Wessberg, J. A  
1009 topographical and physiological exploration of C-tactile afferents and their response to  
1010 menthol and histamine. *Journal of Neurophysiology* **127**, 463-473 (2022).
- 1011 89 Nordin, M. Low-threshold mechanoreceptive and nociceptive units with unmyelinated  
1012 (C) fibres in the human supraorbital nerve. *The Journal of physiology* **426**, 229-240  
1013 (1990).
- 1014 90 Middleton, S. J. *et al.* Nav1. 7 is required for normal C-low threshold mechanoreceptor  
1015 function in humans and mice. *Brain* **145**, 3637-3653 (2022).
- 1016 91 Shea, V. & Perl, E. Sensory receptors with unmyelinated (C) fibers innervating the skin  
1017 of the rabbit's ear. *Journal of neurophysiology* **54**, 491-501 (1985).
- 1018 92 Yang, L. *et al.* Human and mouse trigeminal ganglia cell atlas implicates multiple cell  
1019 types in migraine. *Neuron* **110**, 1806-1821. e1808 (2022).
- 1020 93 Wang, K., Lau, T. Y., Morales, M., Mont, E. K. & Straus, S. E. Laser-capture  
1021 microdissection: refining estimates of the quantity and distribution of latent herpes  
1022 simplex virus 1 and varicella-zoster virus DNA in human trigeminal Ganglia at the  
1023 single-cell level. *Journal of virology* **79**, 14079-14087 (2005).
- 1024 94 Bautista, D. M. *et al.* TRPA1 mediates the inflammatory actions of environmental  
1025 irritants and proalgesic agents. *Cell* **124**, 1269-1282 (2006).
- 1026 95 Macpherson, L. J. *et al.* Noxious compounds activate TRPA1 ion channels through  
1027 covalent modification of cysteines. *Nature* **445**, 541-545 (2007).
- 1028 96 Chesler, A. T. *et al.* The role of PIEZO2 in human mechanosensation. *New England*  
1029 *Journal of Medicine* **375**, 1355-1364 (2016).
- 1030 97 Shaikh, S., Nagi, S. S., McGlone, F. & Mahns, D. A. Psychophysical investigations into

- 1031 the role of low-threshold C fibres in non-painful affective processing and pain  
1032 modulation. *PLoS One* **10**, e0138299 (2015).
- 1033 98 Jørum, E. & Opstad, P.-K. A 4-year follow-up of non-freezing cold injury with cold  
1034 allodynia and neuropathy in 26 naval soldiers. *Scandinavian journal of pain* **19**, 441-451  
1035 (2019).
- 1036 99 Qi, L. *et al.* A DRG genetic toolkit reveals molecular, morphological, and functional  
1037 diversity of somatosensory neuron subtypes. *bioRxiv*, 2023.2004. 2022.537932 (2023).
- 1038 100 Prato, V. *et al.* Functional and molecular characterization of mechanoinensitive “silent”  
1039 nociceptors. *Cell reports* **21**, 3102-3115 (2017).
- 1040 101 Boada, M. D. & Woodbury, C. J. Physiological properties of mouse skin sensory neurons  
1041 recorded intracellularly in vivo: temperature effects on somal membrane properties.  
1042 *Journal of neurophysiology* **98**, 668-680 (2007).
- 1043 102 Buffington, C. T. Visceral pain in humans: lessons from animals. *Current pain and*  
1044 *headache reports* **5**, 44-52 (2001).
- 1045 103 Arcourt, A. *et al.* Touch receptor-derived sensory information alleviates acute pain  
1046 signaling and fine-tunes nociceptive reflex coordination. *Neuron* **93**, 179-193 (2017).
- 1047 104 Xiao, H.-S. *et al.* Identification of gene expression profile of dorsal root ganglion in the  
1048 rat peripheral axotomy model of neuropathic pain. *Proceedings of the National Academy*  
1049 *of Sciences* **99**, 8360-8365 (2002).
- 1050 105 North, R. Y. *et al.* Electrophysiological and transcriptomic correlates of neuropathic pain  
1051 in human dorsal root ganglion neurons. *Brain* **142**, 1215-1226 (2019).
- 1052 106 Martin, M. Cutadapt removes adapter sequences from high-throughput sequencing reads.  
1053 *EMBnet. journal* **17**, 10-12 (2011).

- 1054 107 Dobin, A. *et al.* STAR: ultrafast universal RNA-seq aligner. *Bioinformatics* **29**, 15-21  
1055 (2013).
- 1056 108 Hu, Y. *et al.* Neural network learning defines glioblastoma features to be of neural crest  
1057 perivascular or radial glia lineages. *Science Advances* **8**, eabm6340 (2022).
- 1058 109 Shrikumar, A., Greenside, P. & Kundaje, A. in *International conference on machine*  
1059 *learning*. 3145-3153 (PMLR).
- 1060 110 Huynh-Thu, V. A., Irrthum, A., Wehenkel, L. & Geurts, P. Inferring regulatory networks  
1061 from expression data using tree-based methods. *PloS one* **5**, e12776 (2010).
- 1062 111 Aibar, S. *et al.* SCENIC: single-cell regulatory network inference and clustering. *Nature*  
1063 *methods* **14**, 1083-1086 (2017).
- 1064 112 Vallbo, A., Olausson, H., Wessberg, J. & Kakuda, N. Receptive field characteristics of  
1065 tactile units with myelinated afferents in hairy skin of human subjects. *The Journal of*  
1066 *physiology* **483**, 783-795 (1995).
- 1067 113 Vallbo, Å., Olausson, H. & Wessberg, J. Unmyelinated afferents constitute a second  
1068 system coding tactile stimuli of the human hairy skin. *Journal of neurophysiology* **81**,  
1069 2753-2763 (1999).
- 1070 114 Wasner, G., Schattschneider, J., Binder, A. & Baron, R. Topical menthol—a human  
1071 model for cold pain by activation and sensitization of C nociceptors. *Brain* **127**, 1159-  
1072 1171 (2004).

1073

1074

1075

1076

1077

1078

1079

1080

1081

1082

1083

1084

1085

1086

1087

1088

1089

1090 **Acknowledgements:**

1091 We thank all tissue donors and their families for the generous donations. The new knowledge  
1092 pieces generated from this study would not be possible without their precious gifts. We thank  
1093 NDRI for helping with hDRG procurement, Dr. Isaac Chen, Ms. Arianna Unger, and other  
1094 members at the UPenn (University of Pennsylvania) department of neurosurgery for helping with  
1095 patient DRG procurement for method optimization, the UPenn Skin Biology and Disease Re-  
1096 source-based Center (SBDRC) for helping with laser capture microdissection, and the Children's  
1097 Hospital of Philadelphia (CHOP) Center for Applied Genomics (CAG) for helping with sequenc-  
1098 ing. We thank Dr. Yulong Li for his encouragement in starting this new research direction and all  
1099 lab members in the Luo and Ma labs for their helps in conducting this project. This project is

1100 supported by an internal funding from UPenn to Dr. Luo. Dr. Luo is also supported by NIH  
1101 fundings (R01 (R01NS083702), R34 (NS118411), U01 (EY034681), and P30 (AR069589)). Dr.  
1102 Ernfors is supported by the Swedish Research Council (2019-00761), Knut and Alice  
1103 Wallenbergs Foundation, ERC advanced grant (PainCells 740491). Dr. Olausson is supported by  
1104 Knut and Alice Wallenberg Foundation (grants KAW 2019.0047 and KAW 2019.0487). Dr.  
1105 Nagi is supported by the Swedish Research Council (2021-03054), Swedish Medical Society  
1106 (SLS), and ALF Grants, Region Östergötland.

1107

1108

1109

1110

1111

1112

### 1113 **Materials and Methods:**

#### 1114 *Human tissues and subjects*

1115 Human DRG tissues were procured from National Disease Research Interchange (NDRI). The  
1116 research application was approved by the NDRI Feasibility Committee (RLUW1 01). Six DRGs  
1117 between T11 to L5 of three human donors aged from 23- 61 years were used in this study. The  
1118 dissected DRG tissues from human donors were immediately imbedded in OCT, shipped to the  
1119 Luo lab on dry ice and stored in -80 °C until use. The information of DRGs and dis-identified  
1120 donors and screening criteria are summarized in the Supplementary Tables 1 & 2. As determined  
1121 by the University of Pennsylvania IRB, this study was exempted from the human subject re-  
1122 quirements for the Luo lab.

1123

1124 The human skin biopsies were extracted from three healthy donors at the college of medicine,  
1125 University of Florida. This tissue procurement was approved by the university IRB (protocols  
1126 IRB201500232 and IRB202300291). The information of human skin biopsies and dis-identified  
1127 donors is summarized in the Supplementary Table 3. These three donors are members of one  
1128 family and have no noticeable abnormal somatosensation or peripheral neuropathy. All partici-  
1129 pants were provided written informed consent and signed the document.

1130

1131 *In vivo* recordings of peripheral sensory afferents of healthy human subjects were performed at  
1132 Linköping University, Sweden. These subjects were recruited through social media. All partici-  
1133 pants were provided written informed consent before the start of the experiment. The study was  
1134 approved by the ethics committee of Linköping University (dnr 2020-04426) and complied with  
1135 the revised Declaration of Helsinki.

1136

#### 1137 *Laser capture microdissection of hDRG neurons*

1138 The hDRGs imbedded in OCT were cryosectioned (Cryostat Leica Cm1950) into 20  $\mu$ m sections  
1139 and mounted onto Arcturus PEN Membrane Frame Slides (Applied biosystems, LCM0521). One  
1140 of every five consecutive sections was collected for laser capture microdissection to avoid re-  
1141 peated dissection of the soma from the same neuron in different sections. The slides were stored  
1142 in -80 °C until further use.

1143

1144 On the day of laser capture microdissection, the slides were transferred to the SBDRC laser cap-  
1145 ture microdissection (LCM) core on dry ice. Before dissection, the section was briefly stained

1146 with RNase free Arcturus™ Histogene™ staining solution (Applied biosystems, 12241-05) for  
1147 better visualization of neuronal soma: 70% cold EtOH for 30s; Histogene™ staining for 10s; 70%  
1148 cold EtOH for 30s; 95% cold EtOH for 30s; 100% cold EtOH for 30s and air dry for 2min. Then,  
1149 the slide was put onto laser capture microdissection microscope system (Leica LMD6) for the  
1150 neuronal soma dissection. The laser was calibrated, and the laser intensity was adjusted to  
1151 achieve best dissection efficiency. The dissected individual neuronal soma was collected in the  
1152 cap of a 200 µl PCR tube containing 4 µl lysis buffer<sup>26</sup>. The sequencing library was generated  
1153 following Smart-seq2 workflow<sup>26</sup>. The libraries passing through all quality controls were select-  
1154 ed for the final sequencing.

1155

#### 1156 *Sequencing and sequence alignment*

1157 The libraries were pooled together (384 samples for one batch) and sequenced on NovaSeq 6000  
1158 platform by the Children's Hospital of Philadelphia (CHOP) Center for Applied Genomics  
1159 (CAG). Raw sequencing data was demultiplexed with bcl2fastq2 v.2.20 (Illumina) followed by  
1160 Tn5 transposon adapter sequences trimming with Cutadapt<sup>106</sup>. The processed reads were then  
1161 aligned to human genome (GRCh38 GENCODE as the reference genome, and GRCh38.104.  
1162 GTF as the annotation) using STAR v.2.7.9a49<sup>107</sup>. STAR quantMode GeneCounts was used to  
1163 quantify unique mapped reads to gene counts.

1164

#### 1165 *Analysis of single-soma RNA-seq data of hDRG neurons using Seurat and R*

1166 R (version 4.1.2) and Seurat (version 4.0.5) were used for the single-cell RNA-seq analysis. Six  
1167 objects were created from the individual biological replicates. The data were normalized  
1168 (NormalizeData) after which 4500 most variable features were selected (FindVariableFeatures).

1169 To mitigate batch effects between replicates, we used Seurat’s integrated analysis approach that  
1170 transforms datasets into a shared space using pairwise correspondences (or “anchors”)<sup>19</sup>. An-  
1171 chors were first defined using FindIntegrationAnchors (dims`=`1:30) and the data were then  
1172 integrated (IntegrateData) and scaled (ScaleData), followed by principal component analysis  
1173 (PCA) (RunPCA, npcs`=`50). For clustering, the final parameters were: RunUMAP, reduc-  
1174 tion`=`pca, dims`=`1:25; FindNeighbors, reduction`=`pca, dims`=`1:25; FindClusters,  
1175 resolution`=`3.4. Highly similar clusters without clearly distinguishable markers were merged  
1176 to produce the final 16 clusters.

1177

### 1178 *Analysis of single-soma RNA-seq data of hDRG neurons using Conos*

1179 For Conos<sup>31</sup> analysis, single-soma hDRG data were integrated using CCA space  
1180 `$buildGraph(k=8, k.self=3, space="CCA", ncomps=30, n.odgenes=2000, ver-`  
1181 `bose=TRUE, snn=T, snn.k=10)`. For human single-soma and human single-nucleus dataset,  
1182 co-integration was performed as `$buildGraph(k=8, k.self=3, space="CCA",`  
1183 `n.odgenes=2000, verbose=TRUE, snn=T, snn.k=10)`. For Conos co-clustering mouse  
1184 (Sharms) dataset was downsampled to max 300 cells per cluster, co-integration was performed as  
1185 `$buildGraph(k=8, k.self=3, space="CCA", n.odgenes=2000, verbose=TRUE,`  
1186 `snn=T, snn.k=10)`. Macaque (Kupari, SmartSeq2 dataset) was used for interspecies analysis.  
1187 For Conos co-clustering macaque/human graph was built as `$buildGraph(k=4, k.self=3,`  
1188 `space="CCA", ncomps = 30, n.odgenes=2000, snn=F, snn.k=10)`. For all UMAP plots in  
1189 Conos graphs were embedded as: `$embedGraph(method="UMAP", spread=15, seed = 3)`.  
1190 Label propagation (`$propagateLabels`) was run using method “diffusion”.

1191

1192 *Methods used to elucidate cross-species cluster relationships*

1193 We used four different interspecies analysis approaches. First, Conos, which uses graph-based  
1194 dataset integration and was developed to co-cluster and compare datasets originating from differ-  
1195 ent RNA-seq platforms and species (Fig. 2A-B, S5A-B). Second, probabilistic neural network  
1196 analysis which is a variant of machine learning in which learning module is trained with one da-  
1197 taset and then testing other datasets for pattern recognition and probability output<sup>18</sup> (Fig. S5C-D).  
1198 Third, neural network based hierarchical clustering analysis (Fig. S5E). In the hierarchical clus-  
1199 tering analysis, each query neuron types, either human or macaque, is assigned weights of the  
1200 sensory-type associated patterns by a neural network, which was trained with gene patterns in-  
1201 cluding both species specific and shared cross-species features in the different sensory neuron  
1202 types. The weighted gene patterns were then used for dimensional reduction and nearest neigh-  
1203 bor analysis to infer the hierarchical relationship. Finally, we performed transcription factor as-  
1204 sociated gene regulatory network analysis across all three species using genes network modules  
1205 presumably driven by individual transcription factors (Fig.2D). These three methods have differ-  
1206 ent strengths and weaknesses. Conos finds shared principal components between integrated da-  
1207 taset, but some species-specific features may be lost and lead to impaired statistical sufficiency  
1208 during integration and furthermore can be affected by the number of principal components and  
1209 nearest neighbor distance. Machine learning is based on gene expression and is not supervised by  
1210 shared latent space (i.e. common principal components). Each single reference dataset is used to  
1211 train the machine learning module and then tested by the other dataset. Thus, an advantage of  
1212 this method is that at the stage of machine learning, datasets are not integrated, and hence, prob-  
1213 ability calculations are not affected by principal components or nearest distance. Conversely, its  
1214 disadvantage is that since it emphasizes the features of each cell type, the learning accuracy and

1215 reliability depend on the robustness of the reference or training dataset. For the third approach,  
1216 machine learning-based hierarchical clustering, we extracted the weight of cell type-specific fea-  
1217 tures to construct the latent space covering all cell types across species, whether shared or not.  
1218 With this strategy, we tried to obtain sufficient latent space, as compared to Conos, by training  
1219 and predicting every dataset independently and furthermore, parameterization was used to find  
1220 the most robust hierarchical clustering.

1221

1222 *Cell type probabilistic similarity estimation across cell types and the data integration across*  
1223 *species*

1224 The assessment of cell type purity, the probabilistic similarity, and cell-type integration across  
1225 species are performed using packages in a machine learning based single-cell analysis toolkit-  
1226 scCAMEL, released separately at <https://sccamel.readthedocs.io/>.

1227

1228 *Probabilistic similarity estimation across cell types*

1229 The calculation of cell-type probabilistic score has been described in SWAPLINE package<sup>108</sup>.  
1230 Briefly, a vanilla neural network model was built for cell-type classification. To train the model,  
1231 we removed the cell cycle-related genes and then computed the most variable features. In addi-  
1232 tion, we ranked the marker genes for each cell type by two heuristics for the cell-type specificity  
1233 of both fold change and enrichment score change. Subsequently, the ranked marker genes and  
1234 the most variable genes were merged, log-transformed, and scaled by min-max normalization for  
1235 learning models. The frame of the neural network model and the parameters have been described  
1236 in the SWAPLINE package. The learning accuracy of the neural-network classifier was inspect-  
1237 ed against epoch numbers and was estimated by k-fold cross-validation (k = 3). The learning rate

1238 and learning epochs were selected according to the maximum point of the learning curve reach-  
1239 ing the accuracy plateaus. The probabilistic scores from mouse and macaque species against hu-  
1240 man reference were visualized in violin plot.

1241

#### 1242 *Data integration across species*

1243 For the integration task, we applied interpretable neural-network learning. First, we took one  
1244 dataset from the dataset pool. We trained a neural-network classifier by learning the transcrip-  
1245 tional features of each cell-types in this dataset and then calculated the trained cells' probabilistic  
1246 scores against all cell-types. Subsequently, we used all other datasets as query datasets and calcu-  
1247 lated the probabilistic score of every cell in each query dataset via the trained classifier. Then, we  
1248 took another dataset from the dataset pool and repeated the training and prediction. We repeat the  
1249 training and prediction till every dataset has been used as a training reference for the predictions.  
1250 Here, we consider that the probabilistic score of each cell reflects the weighted gene patterns  
1251 representing each trained cell-type. Thus, we merged the probabilistic scores of all cells from all  
1252 trained and predicted datasets for the principal component analysis. The most significant princi-  
1253 pal components were determined by the elbow method and subsequently used as the latent space  
1254 for further downstream analysis. The tree plot was constructed with the parameter of 11 principal  
1255 components, 90 nearest neighbors, and correlation metric. The trained cell-type similarity was  
1256 calculated with the correlation distance and the average/UPGMA linkage and visualized in the  
1257 hierarchical heatmap.

1258

1259 In parallel, we normalized the gene expression by interpretable learning. We transformed the  
1260 gene symbols of each species into the nomenclature in Homo sapiens. We estimated the features'

1261 weights in each reference cell-type by using the DeepLift algorithm<sup>109</sup>. The gene expression of  
1262 each cell that has been learned or predicted in one trained reference dataset, was inferred by the  
1263 matrix multiplication between the features' weights and the cell-type probabilistic scores. And  
1264 the final gene\*cell expression matrix was calculated by the average of non-empty values across  
1265 all datasets. Using this normalized expression matrix, we enriched the mostly co-expressed genes  
1266 via spearman correlation. These co-expressed genes were used for inferring the TF associated  
1267 gene patterns via a modified GENIE3, as described in<sup>110,111</sup>. The result was visualized as a hier-  
1268 archical heatmap.

1269

#### 1270 *Multiplex FISH, confocal microscopy imaging, and quantification*

1271 OCT embedded freshly dissected human lumbar or thoracic DRG tissues were cryosectioned at  
1272 20  $\mu$ m thickness and mounted on glass slides. The slides were stored in  $-80^{\circ}\text{C}$  to preserve  
1273 RNA integrity until use. RNAscope Fluorescent Multiplex Reagent Kit and RNASCOPE probes  
1274 for the targeted genes (Advanced Cell Diagnostics Inc.) were used for *multiplex FISH*.  
1275 RNAscope *in situ* hybridization was performed in accordance with the manufacturer's instruc-  
1276 tions. In brief, fresh frozen hDRG sections were fixed, dehydrated, and treated with protease.  
1277 The sections were then hybridized with the respective target probe for 2 hr at  $40^{\circ}\text{C}$ , followed by  
1278 two to three rounds of signal amplification. The sections were then mounted under coverslips,  
1279 sealed with nail polish, and stored in the dark at  $4^{\circ}\text{C}$  until imaged. A Leica SP5 confocal micro-  
1280 scope was used to capture images and ImageJ was used for image analysis. In some DRG neu-  
1281 rons, accumulation of lipofuscin in part of cells caused strong autofluorescence in all channels.  
1282 These signals were considered as non-specific background (labeled by asterisk) were excluded  
1283 for analysis. (See Fig. S9 for examples). The percentage of each cluster over all DRG neurons

1284 could be a little bit overestimated due to the following two reasons: 1) Some marker genes or  
1285 marker gene combination may also label a small subset of other cell types; 2) An underestima-  
1286 tion in quantification of total neuronal numbers because some cells have neither multiple FISH  
1287 signals nor DAPI (4',6-diamidino-2-phenylindole) nucleus staining signals.

1288

### 1289 *Human skin biopsy extraction, processing, and immunostaining*

1290 Dermal skin punch biopsies were performed as described herein. Briefly, 1 cc of lidocaine was  
1291 injected subdermally at each biopsy location (Supplementary table 3). A total of six, 3 mm der-  
1292 mal skin punch biopsies were performed on each patient. Excised skin was immediately placed  
1293 in 1.5 mL eppendorf tubes containing 4 degree Celsius 4% paraformaldehyde (PFA) solution that  
1294 was freshly prepared on the same day of the skin biopsy procedure. Biopsy tissue was fixed in 4%  
1295 PFA (dissolved in PBS) for exactly four hours at 4 degrees, followed by 2 X 30 minutes washes  
1296 in phosphate buffered saline (PBS) solution, and then cryoprotected using 1XPBS, 30% sucrose  
1297 at 4 degrees. These tissues in cold 1XPBS, 30% sucrose were overnight shipped to the lab of  
1298 Integrated Tissue Dynamics LLC.

1299

1300 The skin biopsies were mounted in OCT and cryosectioned into 14  $\mu$ m sections. Adjacent sec-  
1301 tions were collected by continuous slides. Immunofluorescence in this study was performed us-  
1302 ing combinations of mouse monoclonal anti-human PGP9.5 (Protein Gene Product, CedarLane,  
1303 Burlington, Canada, 31A3, [source UltraClone Ltd, Isle of Wight, UK]; 1:200), sheep polyclonal  
1304 anti-human CGRP, mouse monoclonal anti-human NEFH (Sigma [ab142]; 1:400), rabbit anti-  
1305 human SST (ImmunoStar 20067, Hudson, WI, USA), and anti-human KIT. Slides were  
1306 preincubated in 1% bovine serum albumin and 0.3% Triton X-100 in PBS (PBS-TB) for 30

1307 minutes and then incubated with primary antibodies diluted in PBS-TB overnight in a humid  
1308 atmosphere at 4°C. Slides were then rinsed in excess PBS for 30 minutes and incubated for 2  
1309 hours at room temperature with the appropriate secondary antibodies diluted in PBS-TB. Follow-  
1310 ing secondary antibody incubation, the sections were rinsed for 30 minutes in PBS and  
1311 coverslipped under 90% glycerol in PBS. Images were collected using a 20X objective on an  
1312 Olympus BX51-WI microscope equipped with conventional fluorescence filters (Cy3:528–553  
1313 nm excitation, 590–650 nm emission; Cy2/Alexa 488: 460–500 nm excitation, 510–560 nm  
1314 emission), a Hamamatsu ER, DVC high-speed camera, linear focus encoder, and a 3-axis motor-  
1315 ized stage system interfaced with NeuroLucida software (MBF Bioscience, Essex, VT, USA).

1316

### 1317 *In vivo electrophysiological recording of human peripheral sensory fibers*

1318 Single-unit axonal recordings (microneurography) were performed from the right posterior  
1319 antibrachial cutaneous, radial, or superficial peroneal nerve of 41 healthy participants (19 males  
1320 and 22 females; 19 to 41 years). Participants were comfortably seated in an adjustable chair with  
1321 legs and arms stretched out (and hand pronated), supported by vacuum pillows, and covered in a  
1322 blanket if they reported as feeling cold.

1323

1324 Under real-time ultrasound guidance (LOGIQ P9, GE Healthcare, Chicago, IL, USA), the target  
1325 nerve was impaled with an insulated tungsten recording electrode (FHC Inc., Bowdoin, ME,  
1326 USA). Adjacent to that, an uninsulated reference electrode was inserted just under the skin. A  
1327 high-impedance preamplifier (MLT185 headstage) was attached to the skin near the recording  
1328 electrode and used together with a low-noise high-gain amplifier (FE185 Neuro Amp EX,  
1329 ADInstruments, Oxford, UK). Once the electrode tip was intrafascicular, single LTMRs were

1330 searched for by soft-brush stroking, and single HTMRs were searched for by coarse-brush strok-  
1331 ing, pinching, and hair tugging in the fascicular innervation zone while making minute electrode  
1332 adjustments.

1333  
1334 All recorded afferents were mechanically responsive and divided into subtypes based on estab-  
1335 lished criteria<sup>68,112,113</sup>. Mechanical threshold and receptive field size were determined using  
1336 Semmes-Weinstein monofilaments (nylon fiber; Aesthesio, Bioseb, Pinellas Park, FL, USA).  
1337 Mechanical threshold was defined as the weakest monofilament to which the unit responded to in  
1338 at least 50% of trials. Hair deflection was tested with a small pair of forceps, carefully avoiding  
1339 skin contact while manipulating the hair. Further, force measurements were performed to ensure  
1340 that no skin/hair pulling occurred. Conduction velocity of the recorded afferent was estimated  
1341 from latency responses to surface electrical stimulation of the receptive field (FE180 Stimulus  
1342 Isolator, ADInstruments, Oxford, UK). Electrically and mechanically evoked spikes were com-  
1343 pared on an expanded time scale to confirm they originated from the same unit. Thermal respon-  
1344 siveness was tested by placing a Peltier probe (7.4 x 12.2 mm, T09, QST.Lab, Strasbourg, France)  
1345 onto the receptive field. After recording baseline activity for at least 30 s (with the thermode in  
1346 contact with the receptive field) at a neutral temperature of 30°C, a series of cooling (down to  
1347 0°C) and warming (up to 50°C) stimuli were delivered at 30-s intervals. If needed, the thermode  
1348 was mounted on a stand for better stability.

1349  
1350 To test *TRPV1* expression, capsaicin (Capsina 0.075%, Bioglan AB, Malmö, Sweden) was topi-  
1351 cally applied to the receptive field. After 1 minute, the skin was wiped clean, and the emergence  
1352 of any spontaneous spiking activity from the recorded afferent was monitored. *TRPM8* expres-

1353 sion was tested by placing an ethanol-soaked gauze pad (90% ethanol as control) onto the recep-  
1354 tive field followed by menthol solution (400 mg of 40% L-menthol dissolved in 90% ethanol,  
1355 Sigma-Aldrich, Inc., Schnellendorf, Germany<sup>114</sup>). The gauze pad was covered with an adhesive  
1356 film to prevent the evaporation of ethanol. After 5 minutes, the skin was wiped clean and the  
1357 emergence of any spontaneous spiking activity from the recorded afferent was monitored. Dur-  
1358 ing these procedures, we documented the participants' verbal descriptions of what they felt, and  
1359 if there was no obvious sensation, the procedure was repeated.

1360

1361 Neural activity was sampled at 20 kHz and recorded using the ADInstruments data acquisition  
1362 system (LabChart software v8.1.24 and PowerLab 16/35 hardware PL3516/P, Oxford, UK), then  
1363 exported to Spike2 (v10.13, Cambridge Electronic Design Ltd., Cambridge, UK). Recorded ac-  
1364 tion potentials were carefully examined offline on an expanded time scale. Threshold crossing  
1365 was used to distinguish action potentials from noise with a signal-to-noise ratio of at least 2:1,  
1366 and spike morphology was confirmed by template matching. Recordings were discarded if mul-  
1367 tiple units were present or if spike amplitudes were not distinct from the noise, preventing secure  
1368 action potential identification.

1369

### 1370 **Figure Generation Software**

1371 Figures were generated in Powerpoint (Microsoft Office) and GraphPad Prism (v9, GraphPad  
1372 Software Inc. La Jolla, CA, USA). Some cartoons were made partially in BioRender (BioRender,  
1373 2022, RRID:SCR\_018361).

1374

### 1375 **Data availability**

1376 The raw and processed datasets for the single-soma sequencing of hDRG neurons reported in this  
1377 study will be deposited into Broad Institute Single cell portal  
1378 ([https://singlecell.broadinstitute.org/single\\_cell](https://singlecell.broadinstitute.org/single_cell)) once the manuscript is accepted for publication.

1379 Macaque (Kupari) data is available at

1380 <https://www.ncbi.nlm.nih.gov/geo/query/acc.cgi?acc=GSE165569>

1381 Mouse (Zeisel) DRG data is available at

1382 [http://loom.linnarssonlab.org/clone/Mousebrain.org.level6/L6\\_Peripheral\\_sensory\\_neurons.loom](http://loom.linnarssonlab.org/clone/Mousebrain.org.level6/L6_Peripheral_sensory_neurons.loom).

1383 Mouse (Sharma) DRG data is available at

1384 <https://www.ncbi.nlm.nih.gov/geo/query/acc.cgi?acc=GSE139088>

1385

#### 1386 **Code availability**

1387 Any custom code will be deposited to Github once the manuscript is accepted for publication.

1388 All analyses are based on previously published code and software.

1389

1390

1391

1392

1393

1394

1395

1396

1397

1398

1399

1400

1401

1402

1403

1404

1405

1406

1407

1408

1409 **Figure 1. Developing a novel laser capture microdissection (LCM) based approach for sin-**  
1410 **gle-soma deep RNA-seq of hDRG neurons**

1411 (A) A diagram shows the overall workflow of this study. (left) A cartoon illustrates features as-  
1412 sociated with different strategies for single-cell RNA-seq of hDRG neurons. (Middle) One real  
1413 example of the laser dissection of a hDRG neuron soma is shown. (Right) Analyses and experi-  
1414 ments conducted in this study are summarized. Scale bar, 50  $\mu\text{m}$  (cell) and 500  $\mu\text{m}$  (cap)

1415 (B) UMAP plot showing the clusters of 1066 hDRG neurons. (C-D) Violin plots showing total  
1416 number of detected genes (C) and the expression of neuronal marker *SLC17A6* (D). (E) The  
1417 grouping clusters based on the soma size, and the expression of *INA*, *NEFH*, *PRDM12*, and  
1418 *CALCA*. (F) UMAPs showing some canonical marker gene expression in each cluster. (G)  
1419 UMAP plot with names of each cluster.

1420

1421 **Fig. 2 Cross-species analysis of DRG neurons in human, macaque, and mouse**

1422 (A, B) Conos label propagation from mouse (Sharma) (A, combined Sharma & Usoskin nomen-  
1423 clature) and macaque (B) to hDRG neuron clusters showing the cell type correlation. For  
1424 UMAPs for correspondent co-integration, from which these results were inferred, see Fig. S5A-  
1425 B. (C) Summary of correspondence of DRG neuron clusters among three species. Solid lines  
1426 depict clear match, and dashed lines represent partial similarity. (D) Heatmap visualization of  
1427 cross-species-conserved and species-specific transcription factor associated gene patterns across  
1428 mouse, macaque, and human. Species are color coded in the right column. Yellow boxes, con-  
1429 served, green boxes, species-specific gene regulatory networks.

1430

1431 **Figure 3. Marker gene expression and validation in C-fiber pruriceptors, thermoreceptors,**  
1432 **and nociceptors**

1433 (A-D) Marker genes for specific labeling of each cluster and validation by multiplex FISH for  
1434 hNP1 and hNP2 (A), hPEP.SST(B), hTRPM8 (C), and hPEP.TRPV1/A1.1 and  
1435 hPEP.TRPV1/A1.2 (D). The fluorescent images show detected transcripts in one example hDRG  
1436 neuron (cell body outlined by the white dashed line. Circle charts next to images show quantifi-  
1437 cation: the arcs indicate the percentage of neurons positive for the given marker gene over all  
1438 sampled DRG neurons. The sector shaded areas indicate the approximate percentage of each cell  
1439 type over the total quantified hDRG neurons. N=2, A (199 neurons total), B (220 neurons total),  
1440 C (156 neurons total), D (202 neurons total). Scale bar, 50  $\mu$ m.

1441

1442 **Figure 4. Marker gene expression and validation in A-fiber nociceptors**

1443 (A-D) Marker genes for specific labeling of each cluster and validation by multiplex FISH for  
1444 hPEP.PIEZO2<sup>h</sup> (A), hPEP.KIT (B), hPEP.CHRNA7 (C), and hPEP.NTRK3 (D). The fluorescent

1445 images show the detected transcripts in one example hDRG neuron (cell body outlined by the  
1446 white dashed line). Circle charts next to images show quantification: the arcs indicate the per-  
1447 centage of neurons positive for the given marker gene over all sampled DRG neurons. The sector  
1448 shaded areas indicate the approximate percentage of each cell type over the total quantified  
1449 hDRG neurons. N=2, A (165 neurons total), B (173 neurons total), C (196 neurons total), D (191  
1450 neurons total). Scale bar, 50  $\mu$ m.

1451

### 1452 **Figure 5. Marker gene expression and validation in C- and A-LTMRs**

1453 (A- D) Marker genes for specific labeling of each cluster and validation by multiplex FISH for  
1454 hC.LTMR (A), hA $\delta$ .LTMR (B), hA $\beta$ .LTMR (C), hPropr (D) and hATF3 (E). The fluorescent  
1455 images show the detected transcripts in one example hDRG neuron (cell body outlined by the  
1456 white dashed line). Circle charts next to images show quantification: the arcs indicate the per-  
1457 centage of neurons positive for the given marker gene over all sampled DRG neurons. The sector  
1458 shaded areas indicate the approximate percentage of each cell type over the total quantified  
1459 hDRG neurons. N=2, A (205 neurons total), B (183 neurons total), C (188 neurons total), D (198  
1460 neurons total), E (202 neurons total). Scale bar, 50  $\mu$ m.

1461

### 1462 **Figure 6. Single-soma deep RNA-seq dataset is powerful for molecular discovery**

1463 (A) Comparison of the total detected number of GPCRs, ion channels, chemokine receptors, and  
1464 neuropeptides in single-soma, spatial, and single-nucleus RNA-seq datasets. (B-C) Expression of  
1465 putative itch receptors in hDRG neurons. Some receptors are highly enriched (B), while some  
1466 receptors are barely detected (C) in human itch populations. (D) Novel GPCRs, ion channels,  
1467 and other genes enriched in human itch populations.

1468

1469 **Figure 7. Molecular profile-informed single-unit microneurography recordings revealed**  
1470 **novel physiological properties of a population of human A-HTMRs.**

1471 (A) Predicted physiological properties of hPEP.KIT sensory afferents based on single-soma deep  
1472 RNA-seq data. (B) Receptive field locations of recorded single afferents from superficial per-  
1473 oneal (S. peroneal), posterior antebrachial cutaneous (PABCN), and radial nerve recordings (n =  
1474 47). (C) Distribution of mechanical (monofilament) thresholds for HTMRs and LTMRs in the  
1475 recorded samples. (D) Individual and mean ( $\pm$ SEM) conduction velocities of different HTMR  
1476 and LTMR types in response to surface electrical stimulation from upper and lower limbs (Field-  
1477 LTMR:  $40.3 \pm 4.2$  m/s, n=2; SA1-LTMR:  $44.9 \pm 2.6$  m/s, n=3; SA2-LTMR:  $44.9 \pm 1.2$  m/s, n=3;  
1478 A-HTMR cooling-:  $50.6 \pm 4.8$  m/s, n=5; A-HTMR cooling+:  $48.9 \pm 5.0$  m/s, n=3; C-LTMR:  $1.0$   
1479  $\pm 0.05$  m/s, n=8; C-HTMR:  $0.7 \pm 0.08$  m/s, n=5). (E) Spike activities of a putative hPEP.KIT  
1480 unit (A-HTMR cooling+) in response to repeated stimulations of the receptive field, superim-  
1481 posed on an expanded time scale. (F-H) Responses of an A-HTMR cooling+ unit to soft and  
1482 coarse brushing (F), heating (G) and cooling (H). (I) Schematic showing the link between the  
1483 histologically identified  $KIT^+/CGRP^+/NEFH^+$  sensory afferents and the molecularly defined  
1484 hPEP.KIT population, likely representing a type of heat/capsaicin-insensitive but cold-sensitive  
1485 A-HTMRs.

1486

1487 **Figure 8. Molecular profile-informed single-unit microneurography recordings revealed**  
1488 **novel physiological properties of a population of human C-LTMRs.**

1489 (A) Novel physiological properties of hC.LTMR sensory fibers predicted based on gene expres-  
1490 sion obtained from the single-soma deep sequencing. (B) Spike activity of a hC.LTMR unit in

1491 response to repeated stimulations of the receptive field, superimposed on an expanded time scale.  
1492 (C) Individual and mean ( $\pm$ SEM) conduction velocities of different HTMR and LTMR types in  
1493 response to surface electrical stimulation from upper and lower limbs (the same plot from Fig.  
1494 7D) (D-H) Responses of a hC.LTMR unit to soft brushing and hair movement (D), cooling (E),  
1495 menthol (F), heating (G) and capsaicin (H). Spike activity of that hC.LTMR before and after  
1496 capsaicin application, overlaid on an expanded timescale (H). Conduction delay was adjusted  
1497 based on the latency of electrically triggered spiking for that recorded afferent. Note, different  
1498 scaling.

# Figure 1

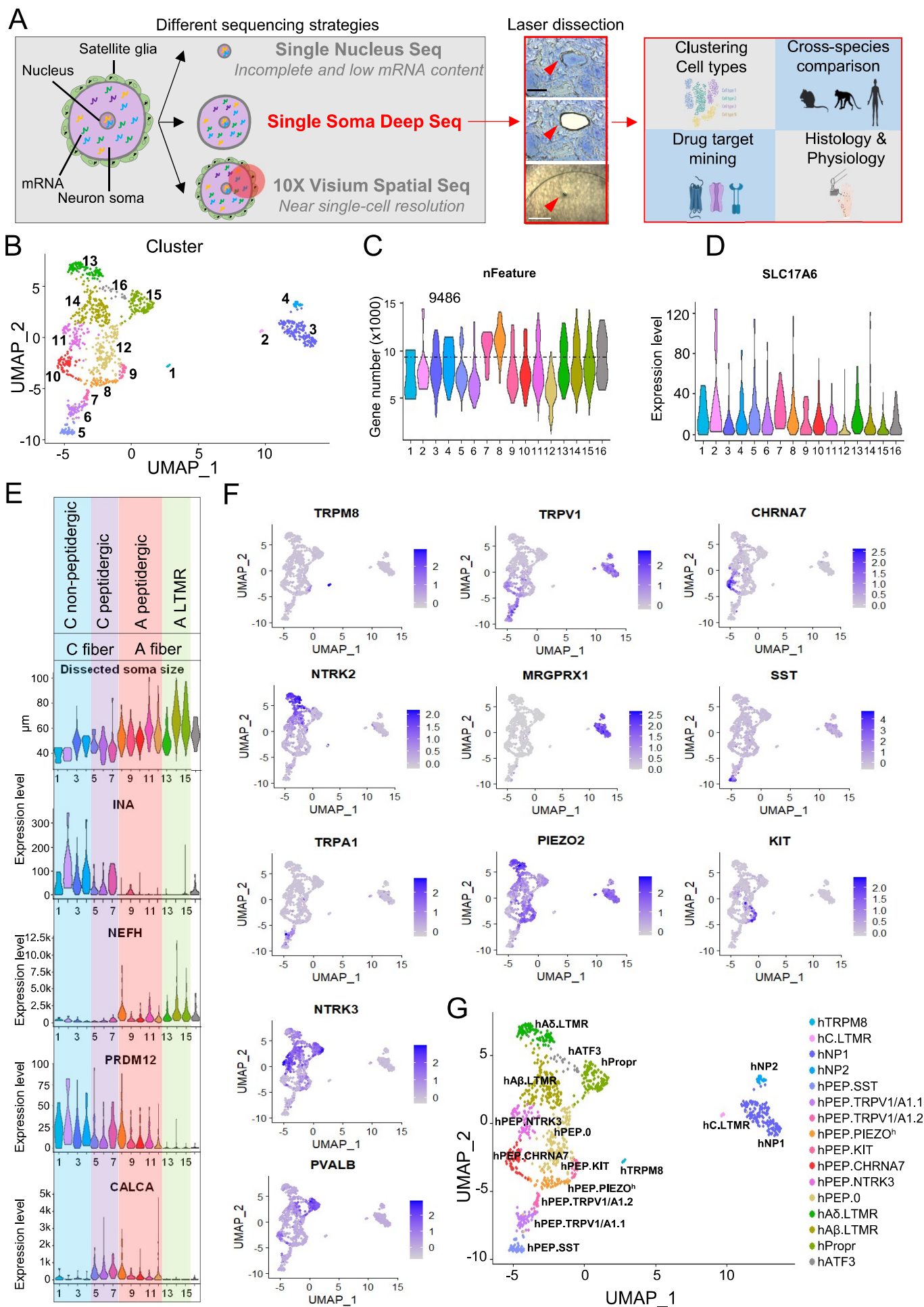


## Figure 2

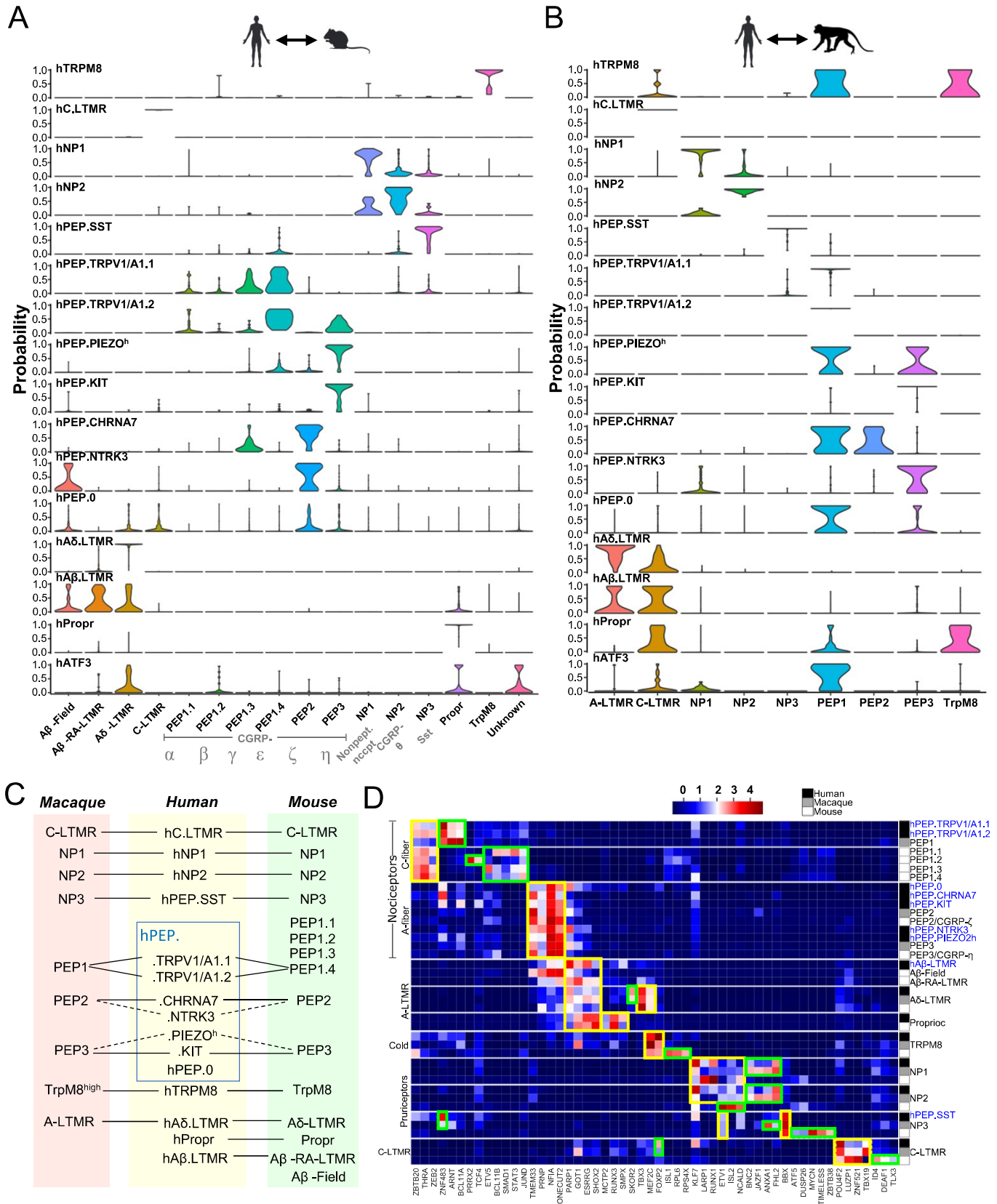


# Figure 3

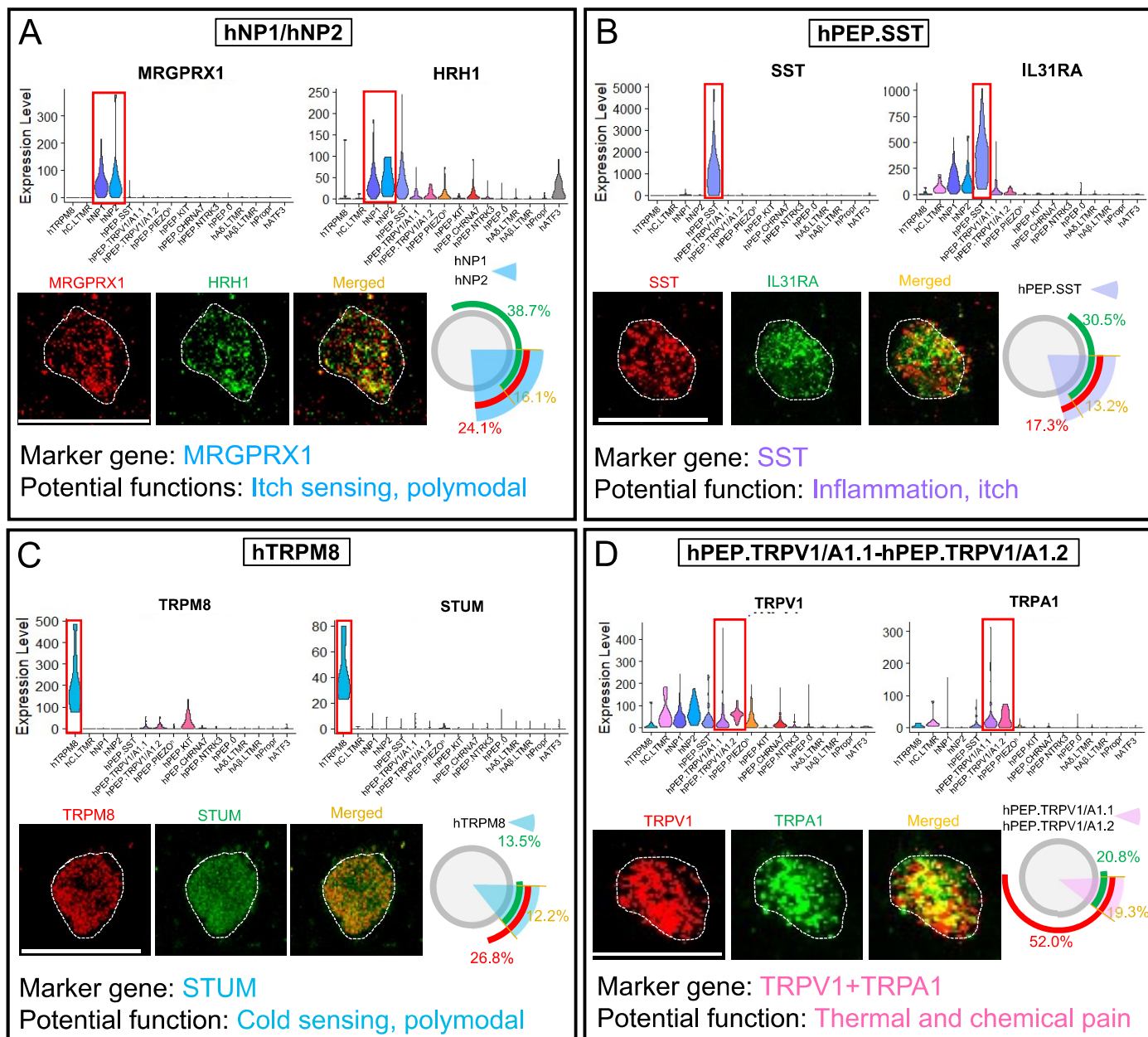


# Figure 4

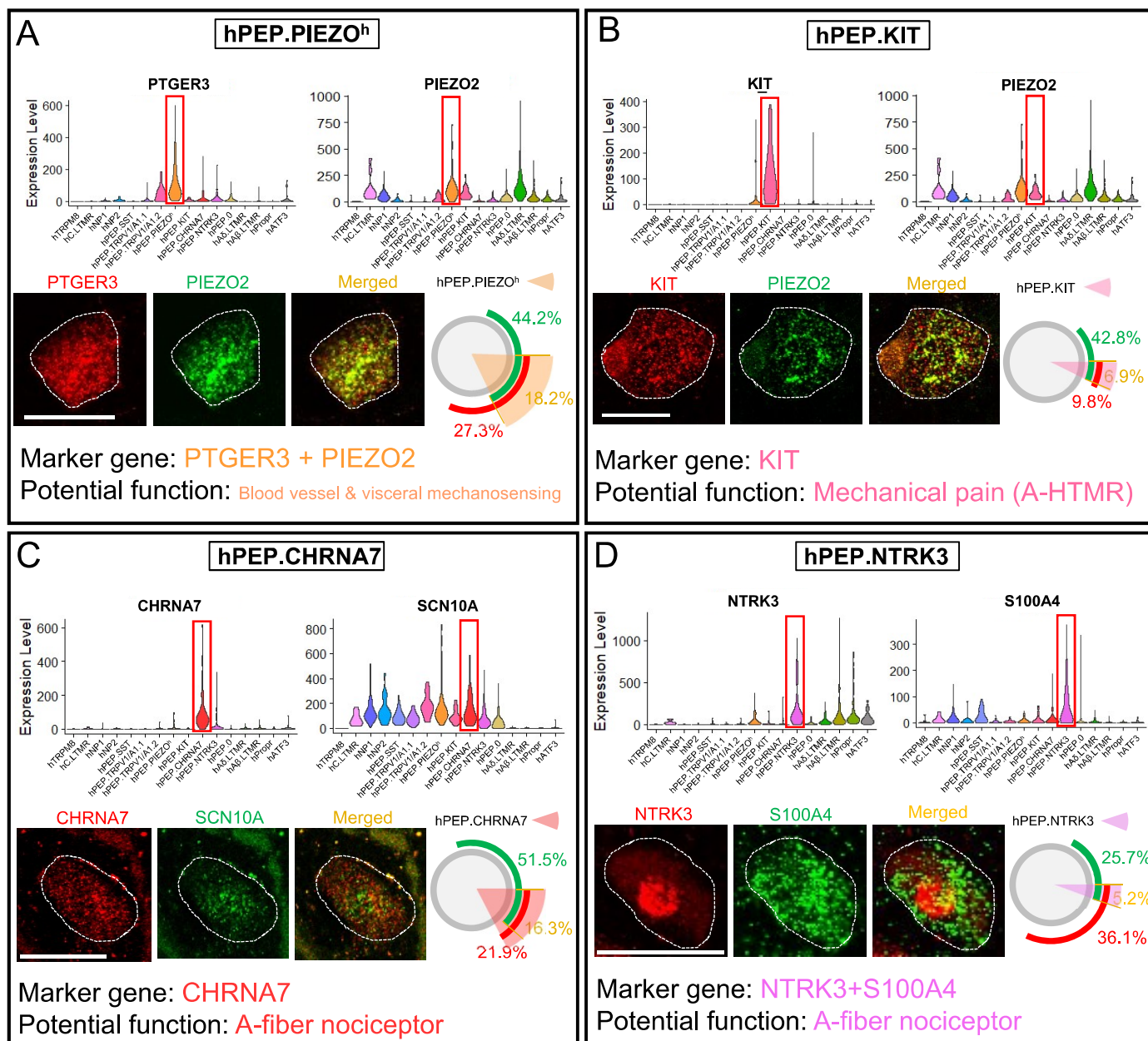


# Figure 5

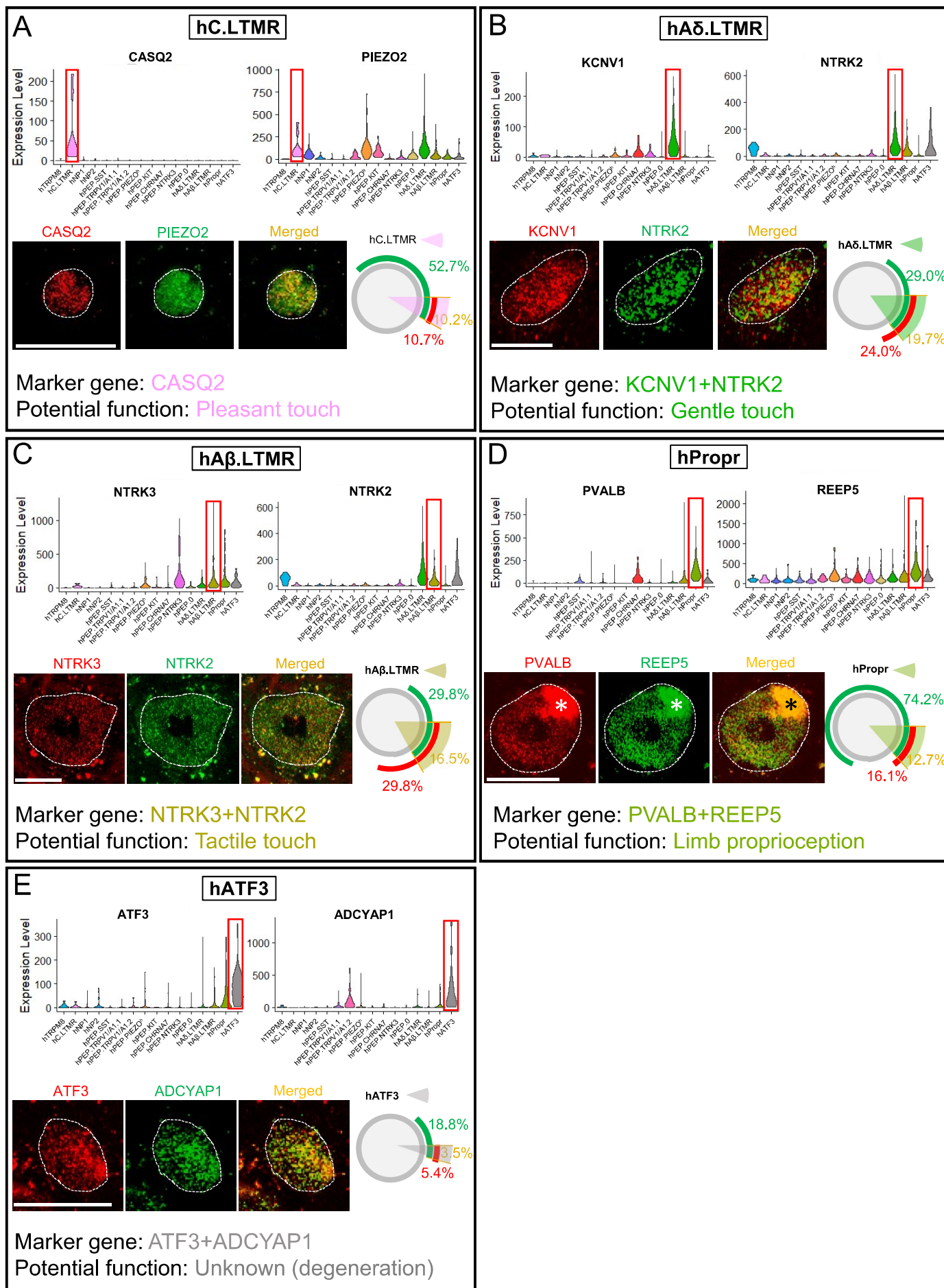
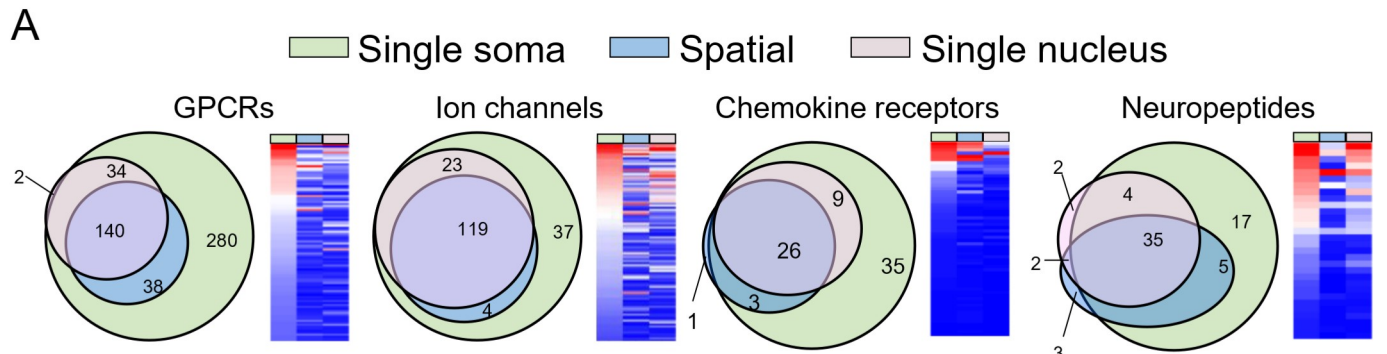
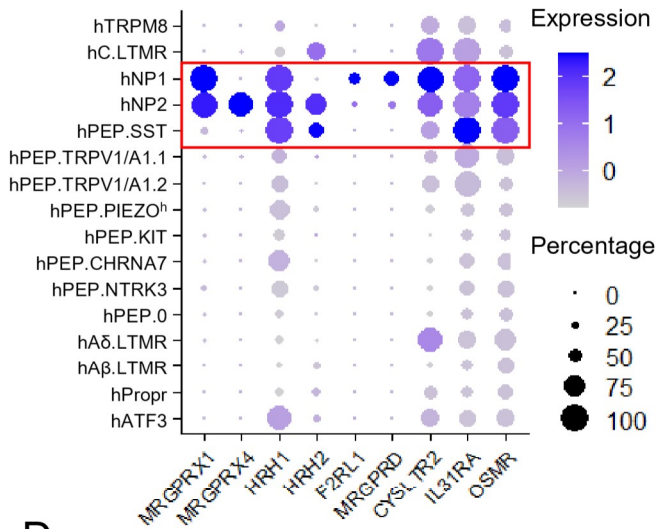


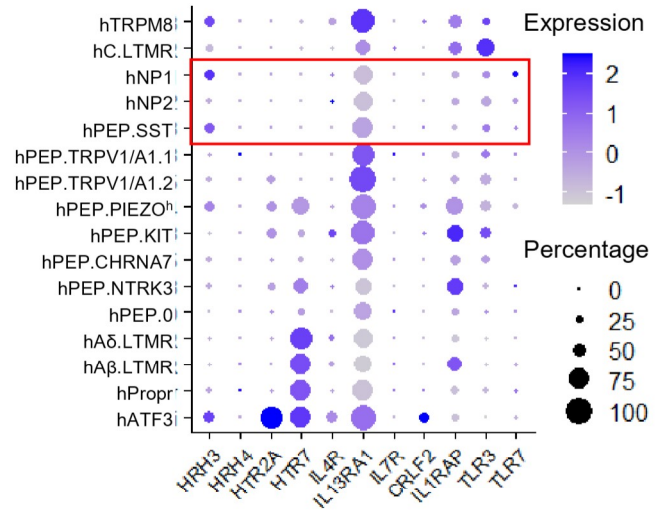
# Figure. 6



**B** Receptors enriched in human itch-sensing DRG neurons



**C** Anti-itch drug targets not enriched in human itch-sensing DRG neurons



**D** Potential novel anti-itch drug targets

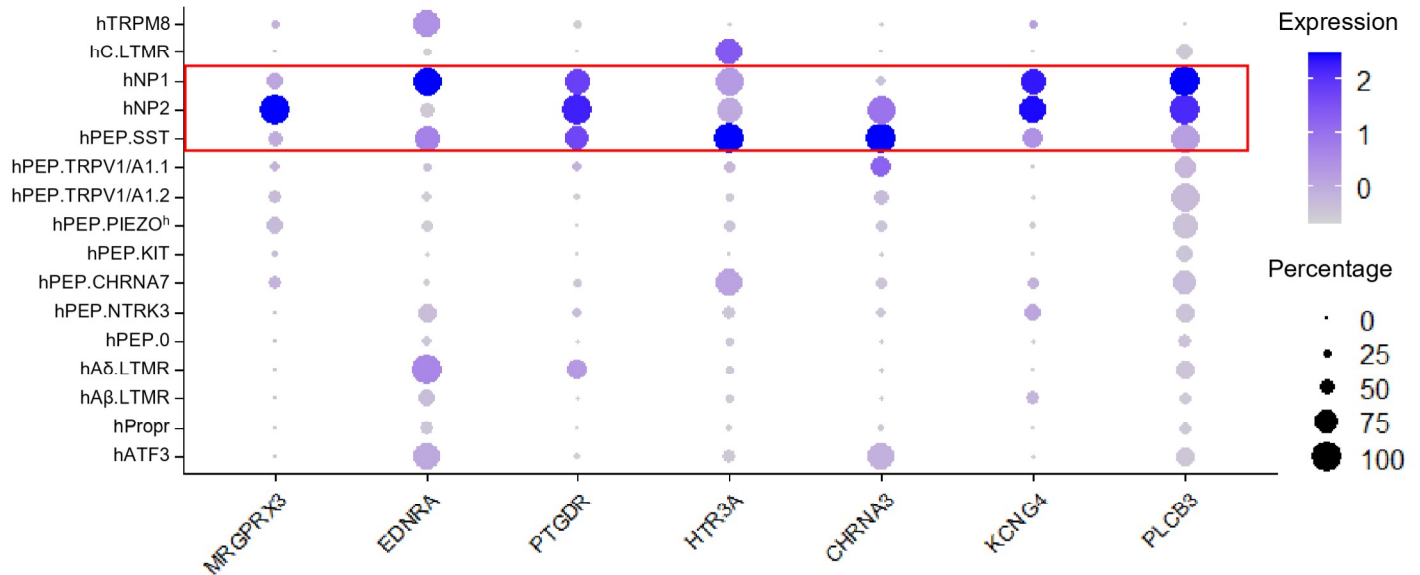


# Figure 7

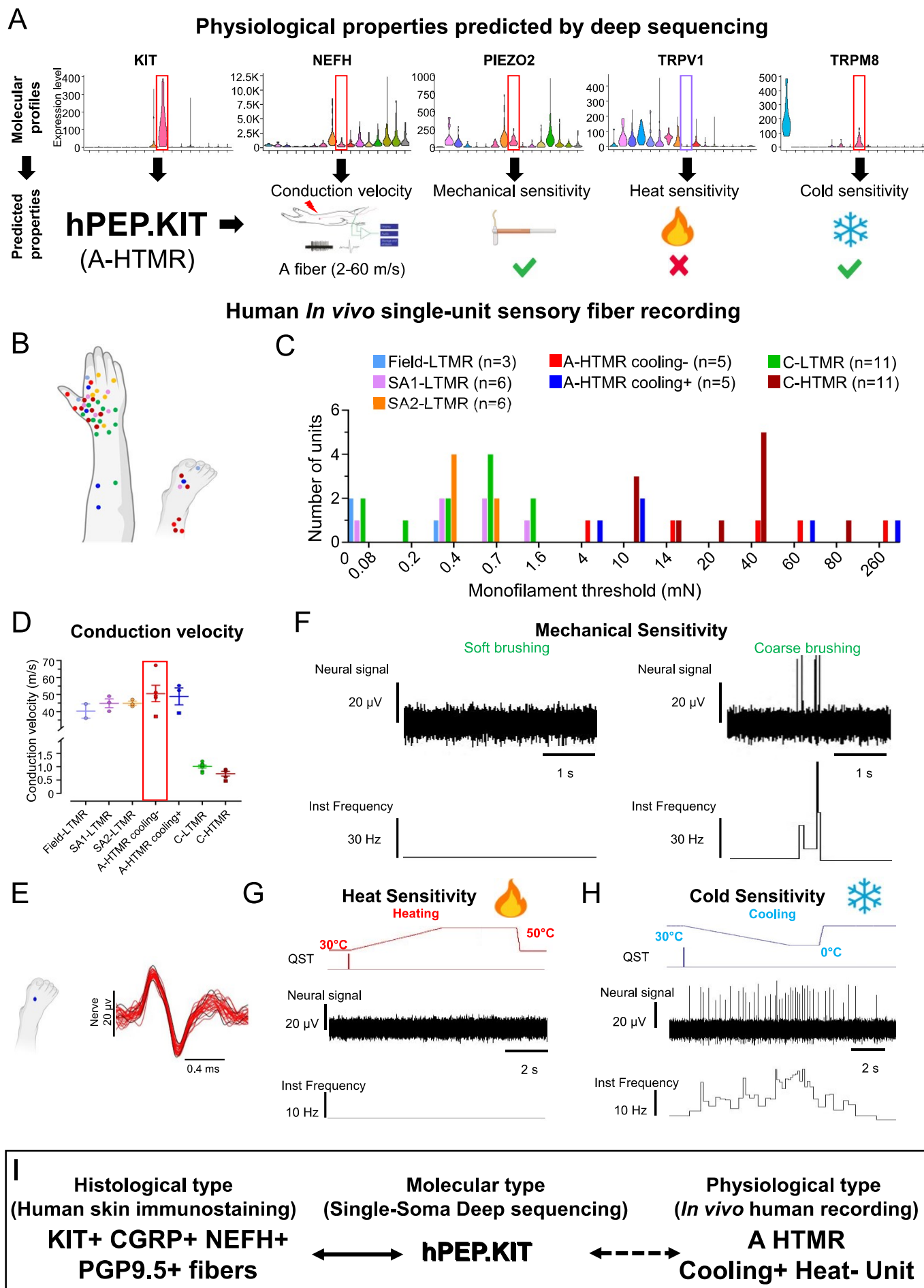
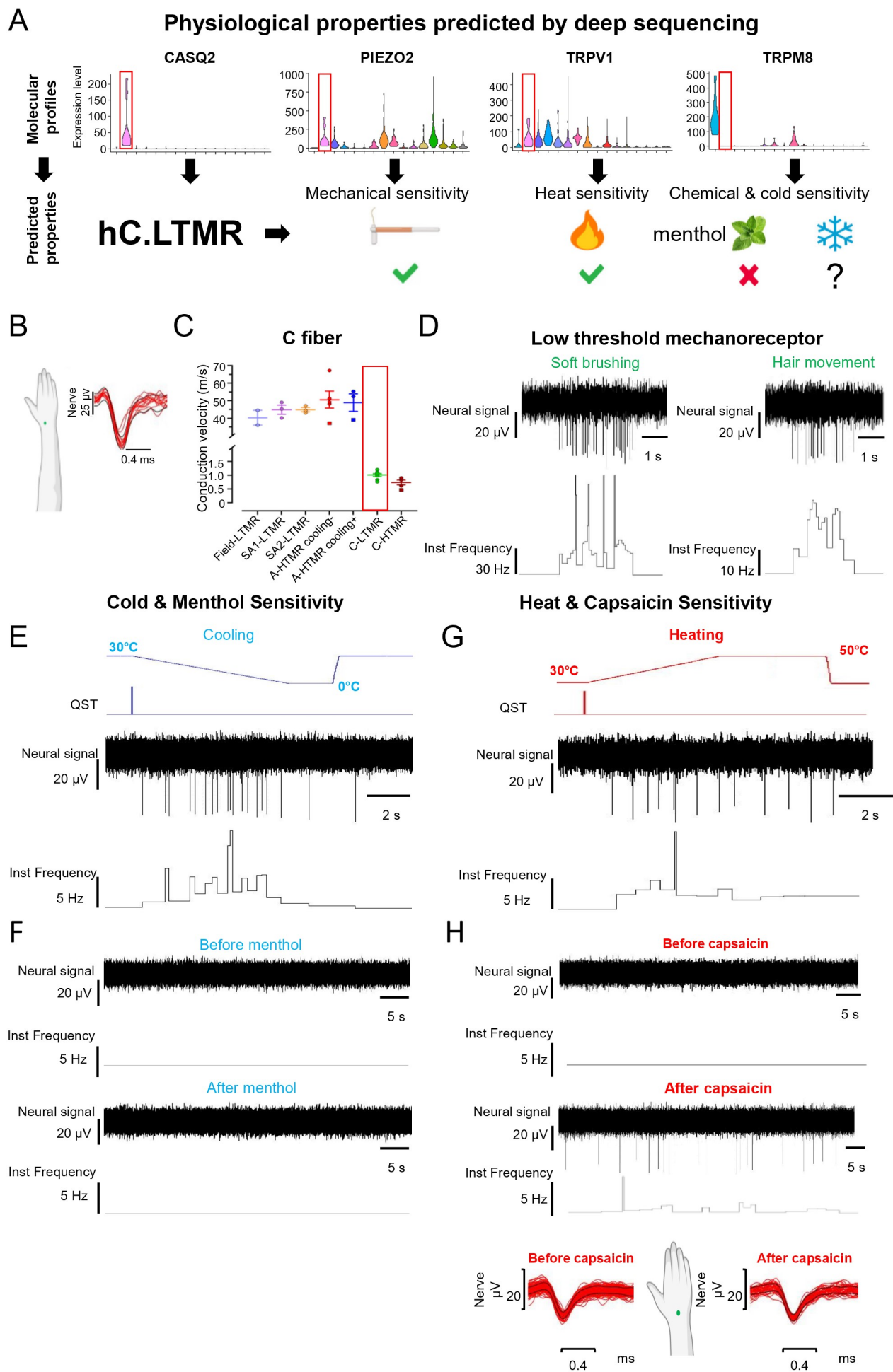
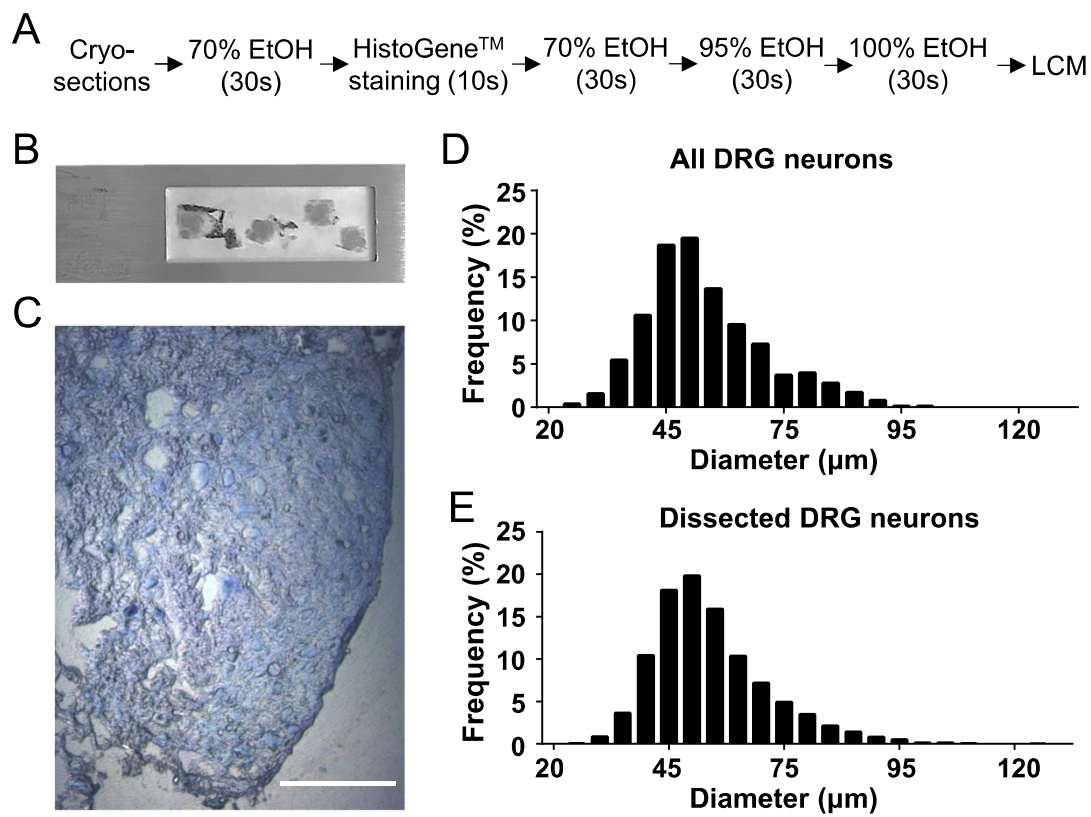


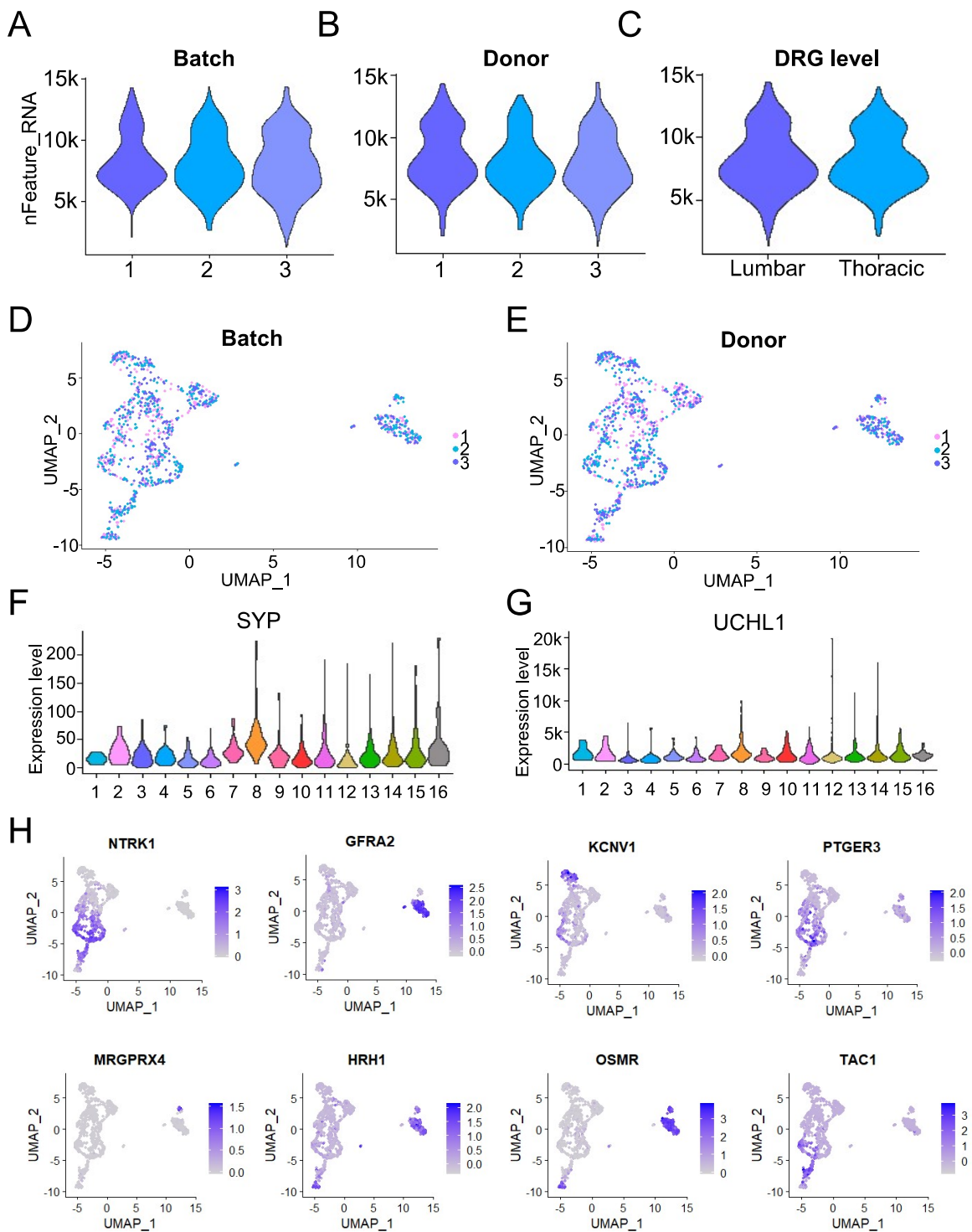
# Figure 8



# Supplementary Figure 1

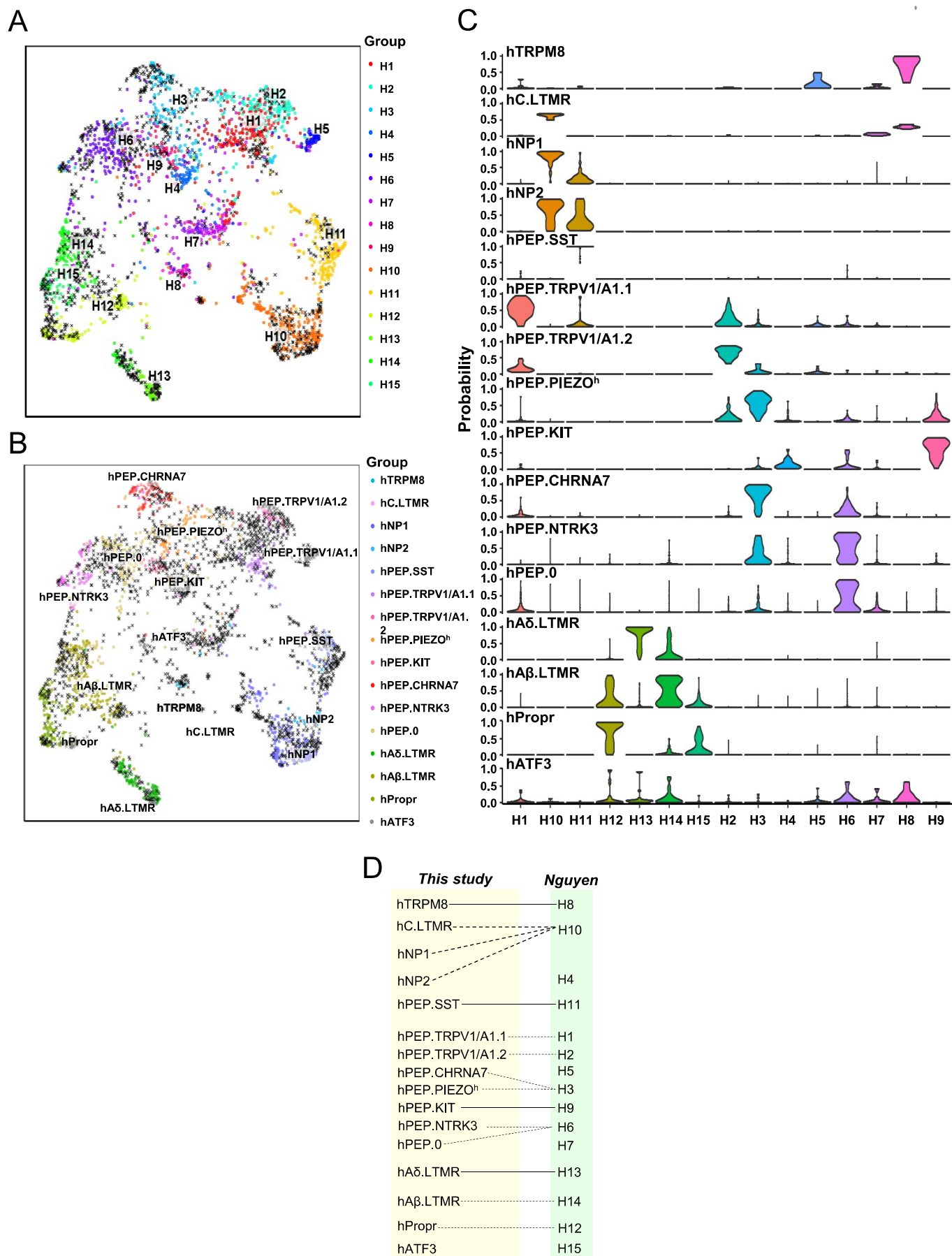


# Supplementary Figure 2

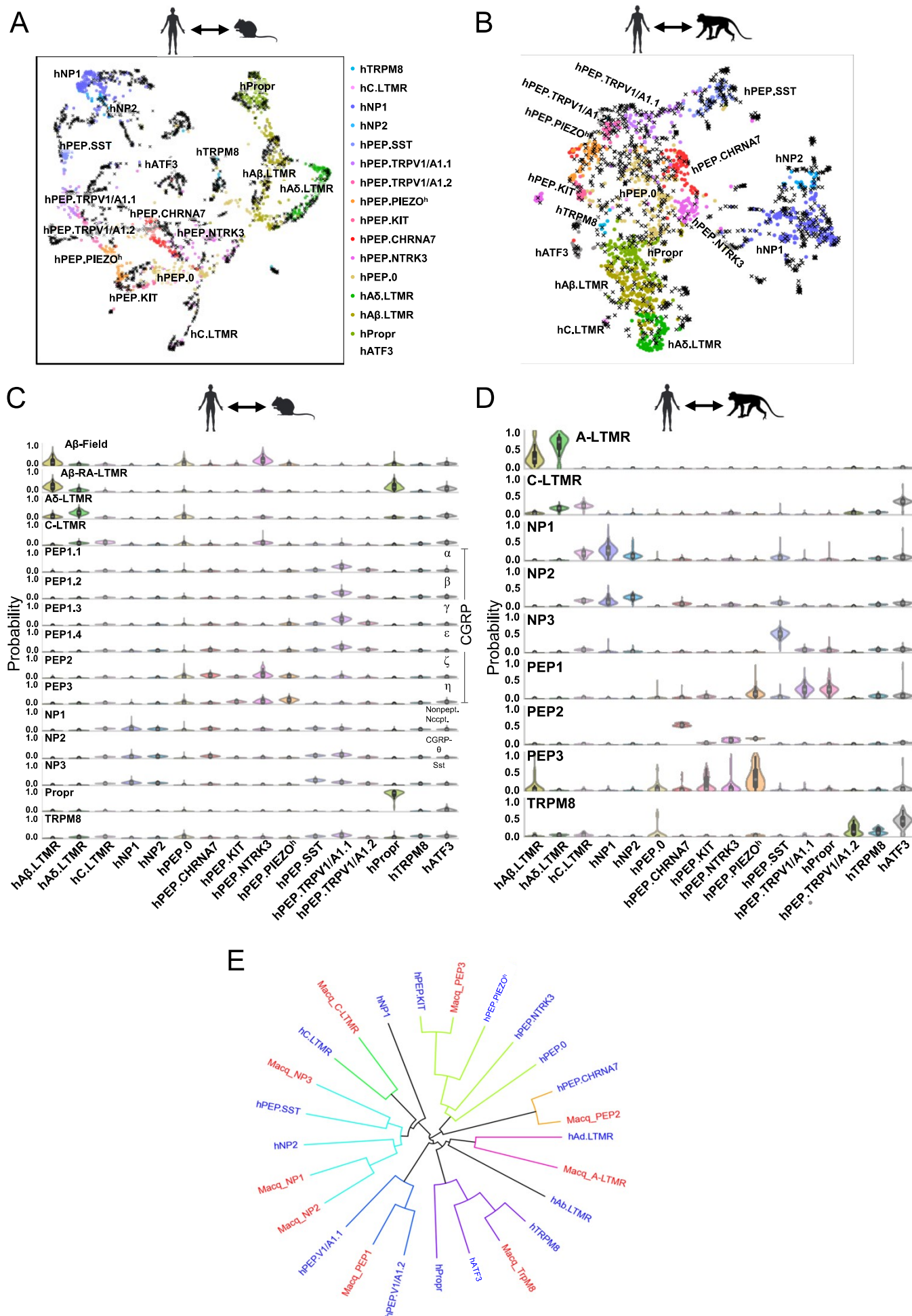




# Supplementary Figure 4

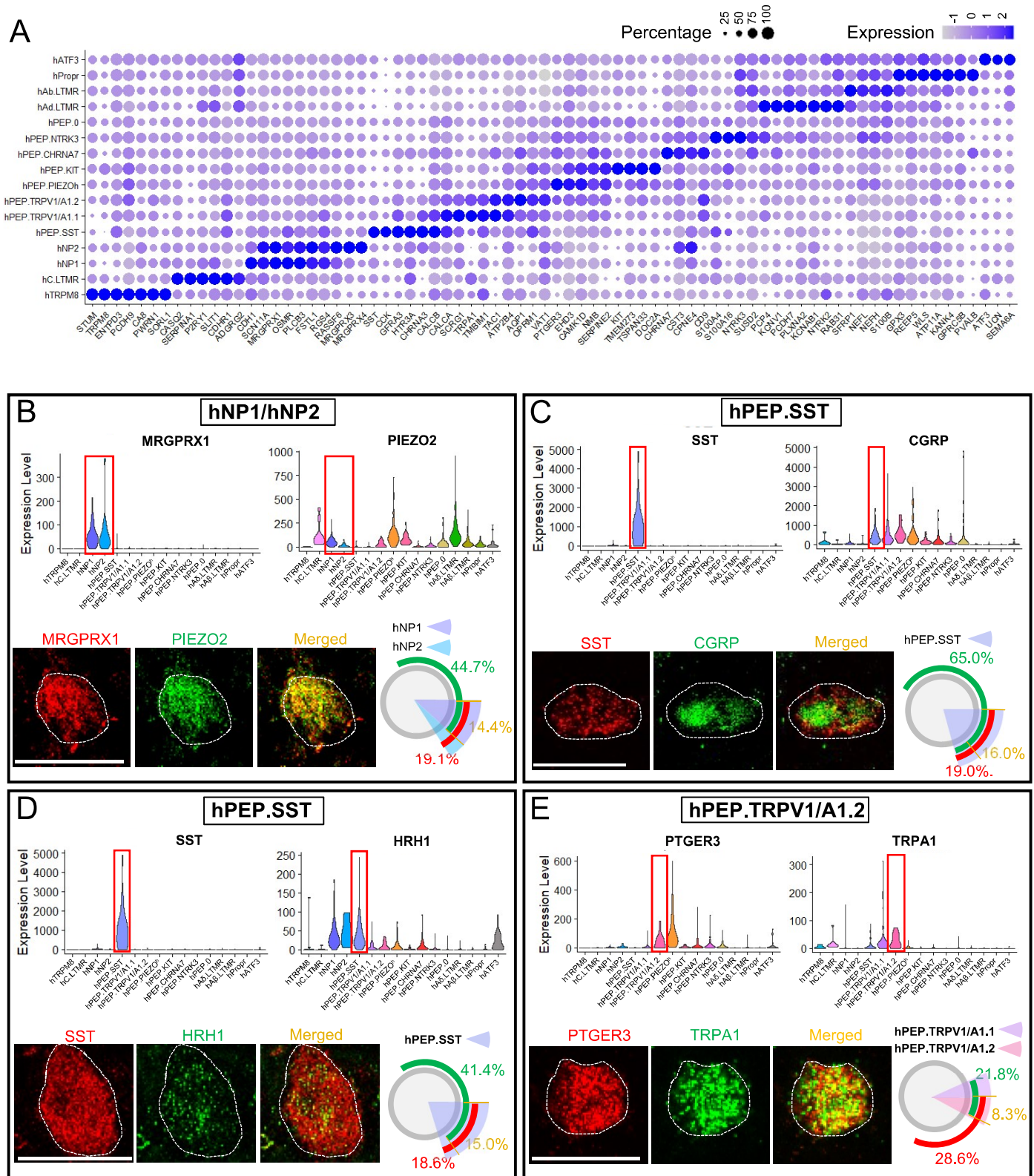


# Supplementary Figure 5



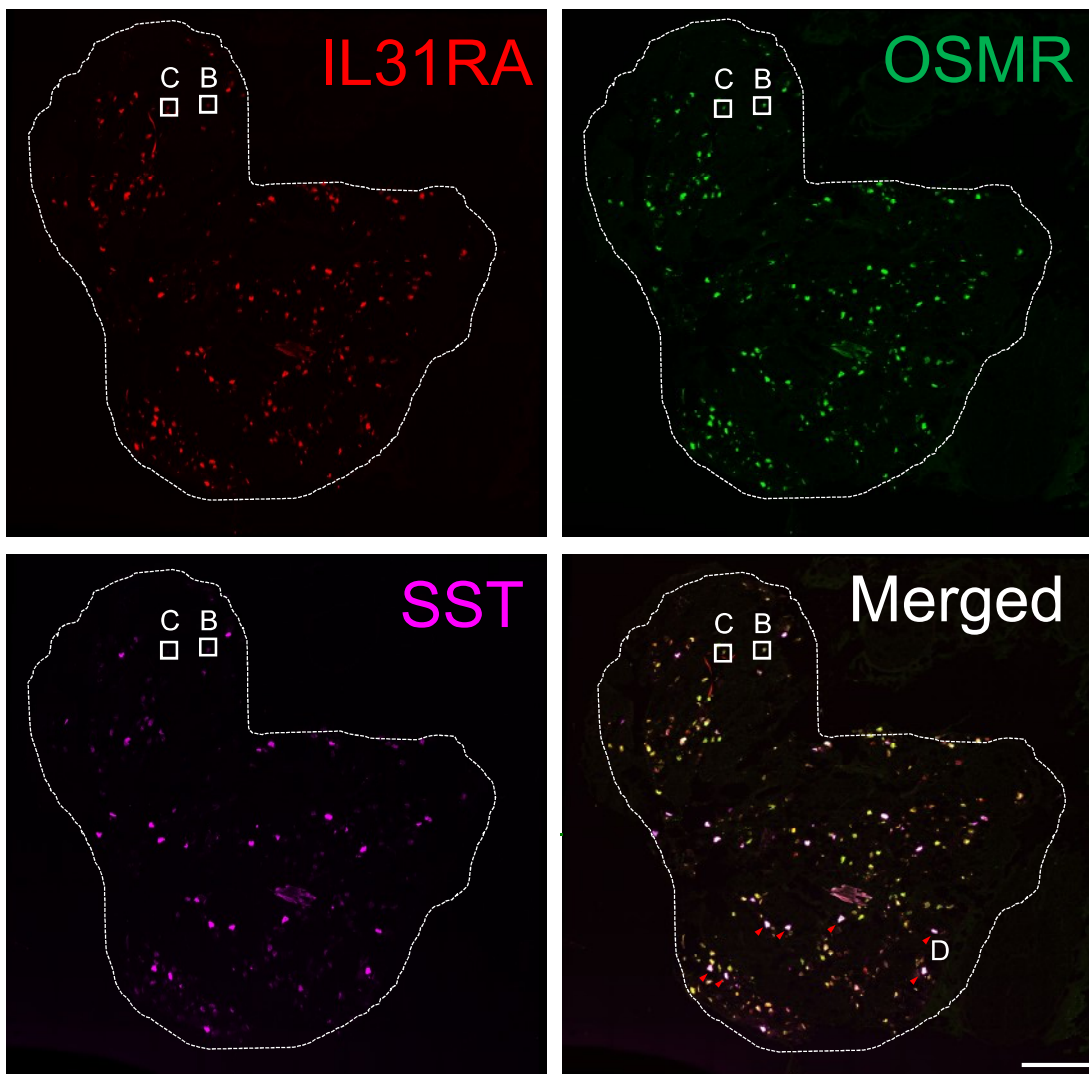


# Supplementary Figure 7

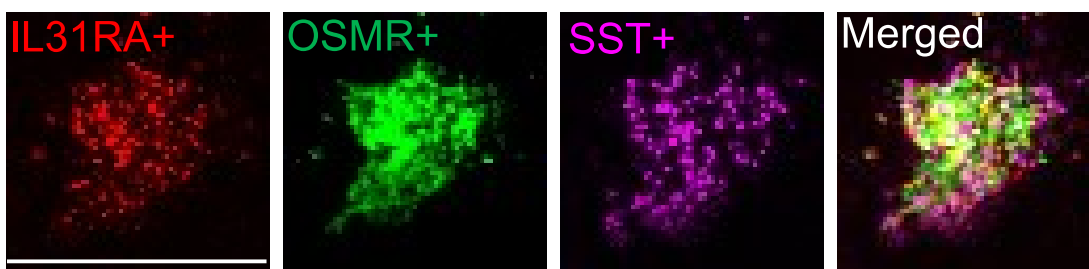


# Supplementary Figure 8

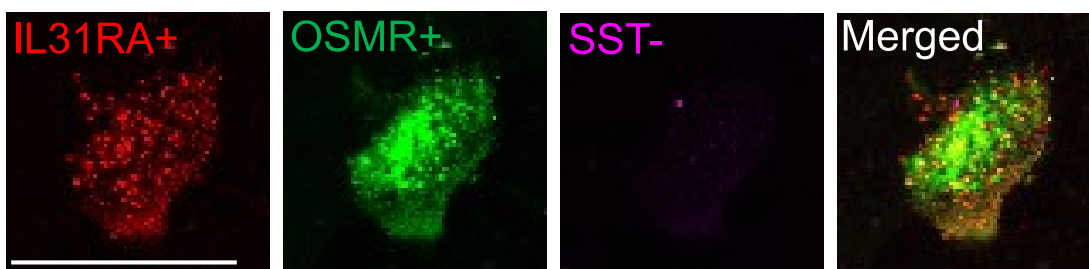
A



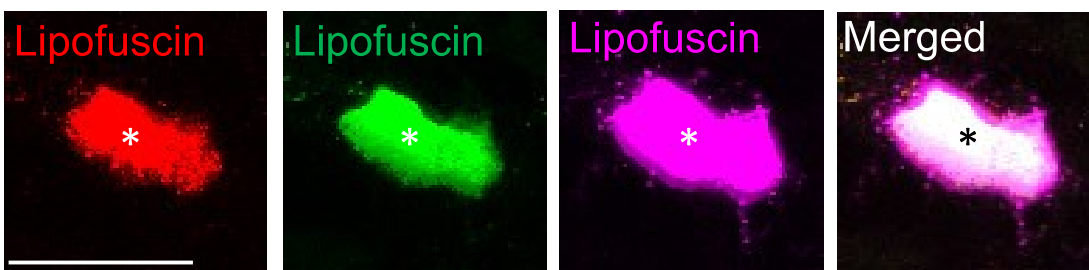
B



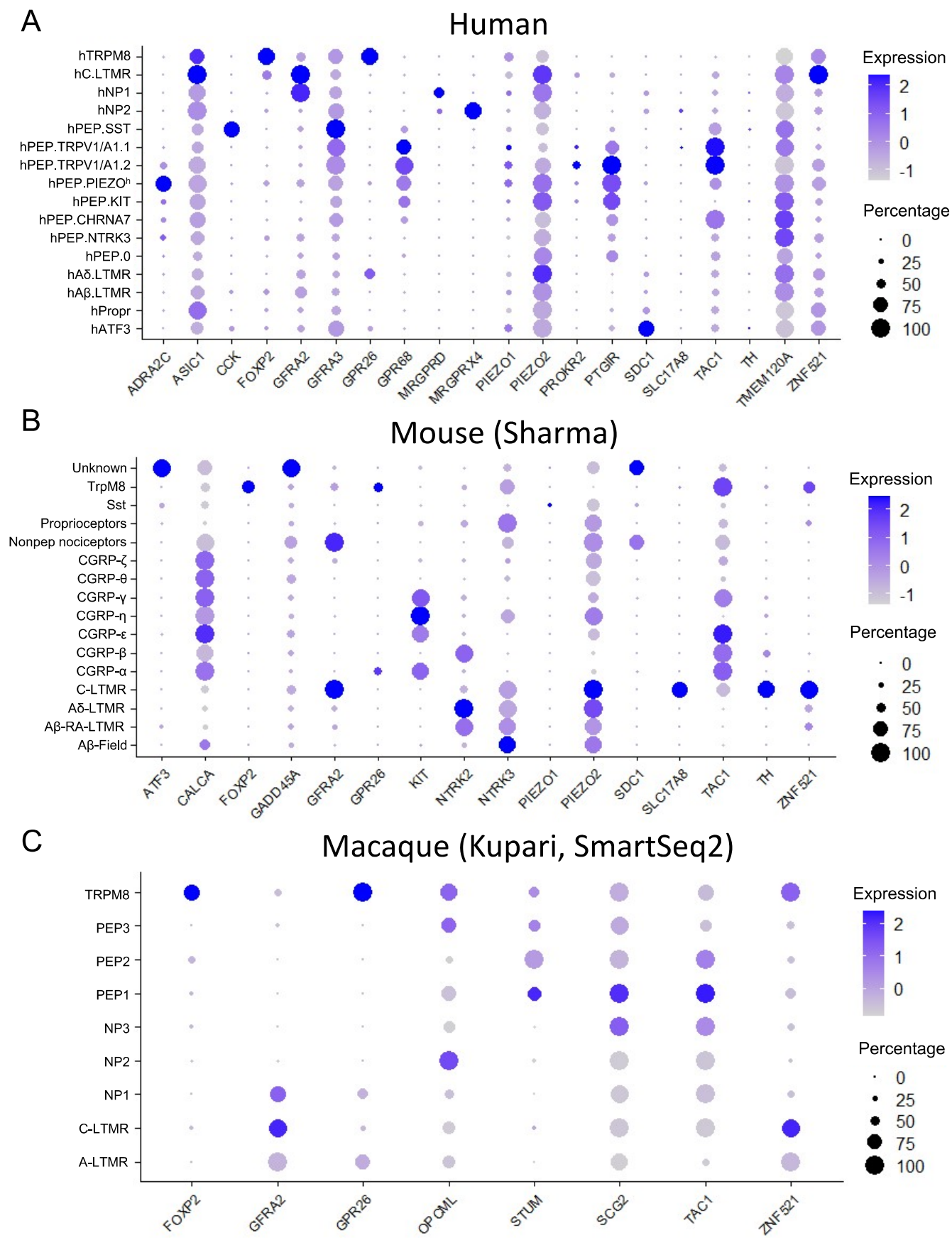
C



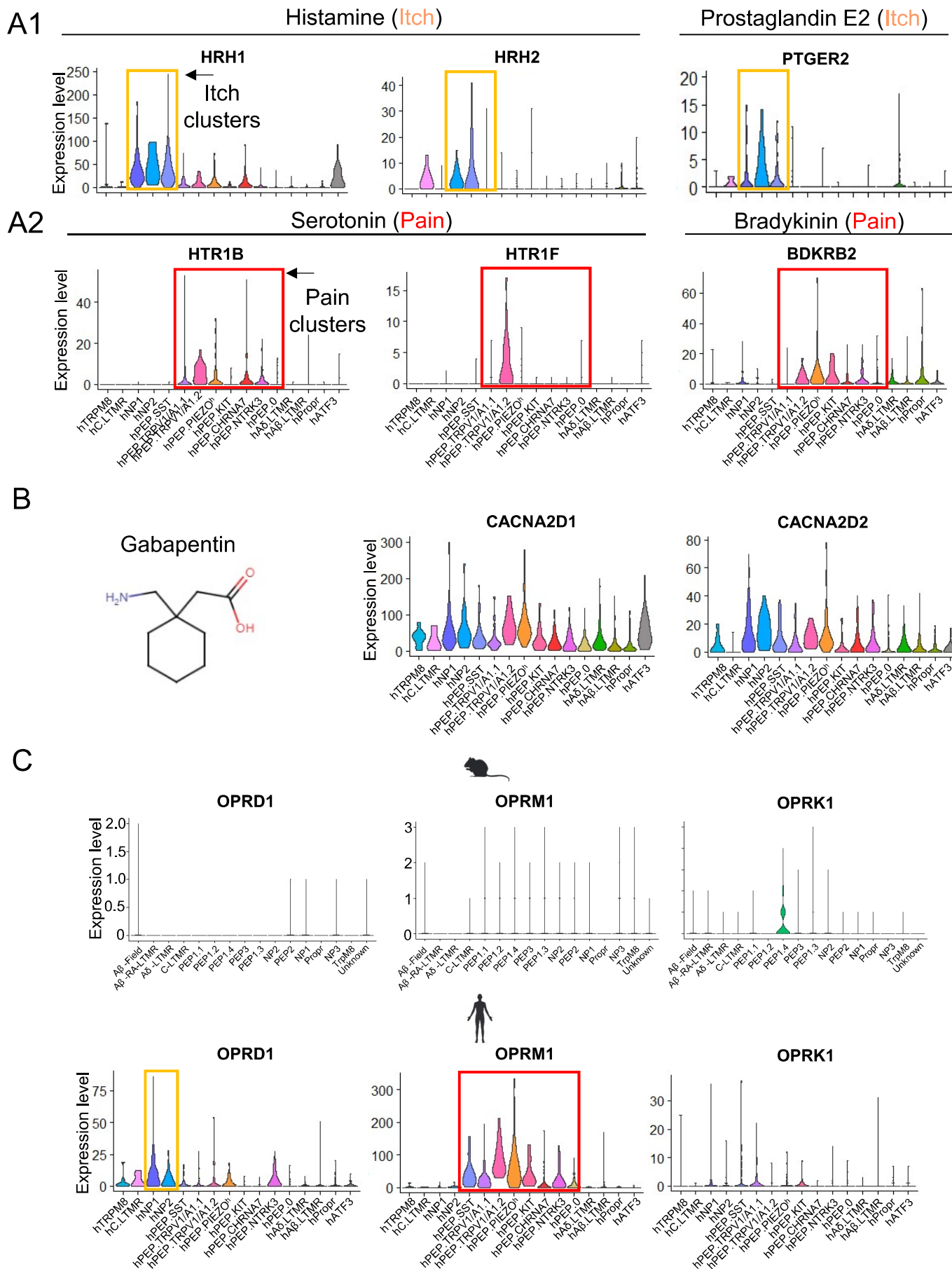
D



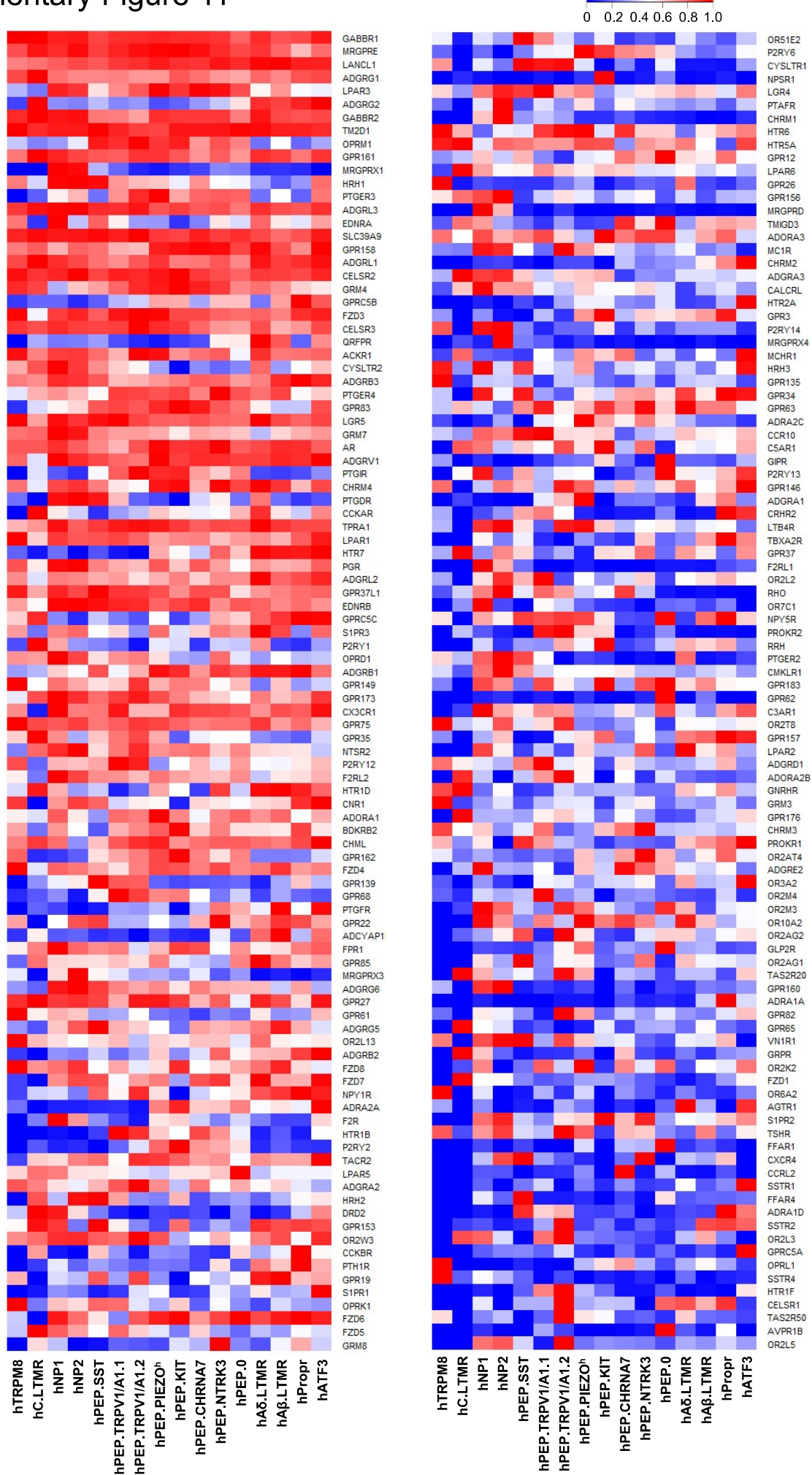
# Supplementary Figure 9



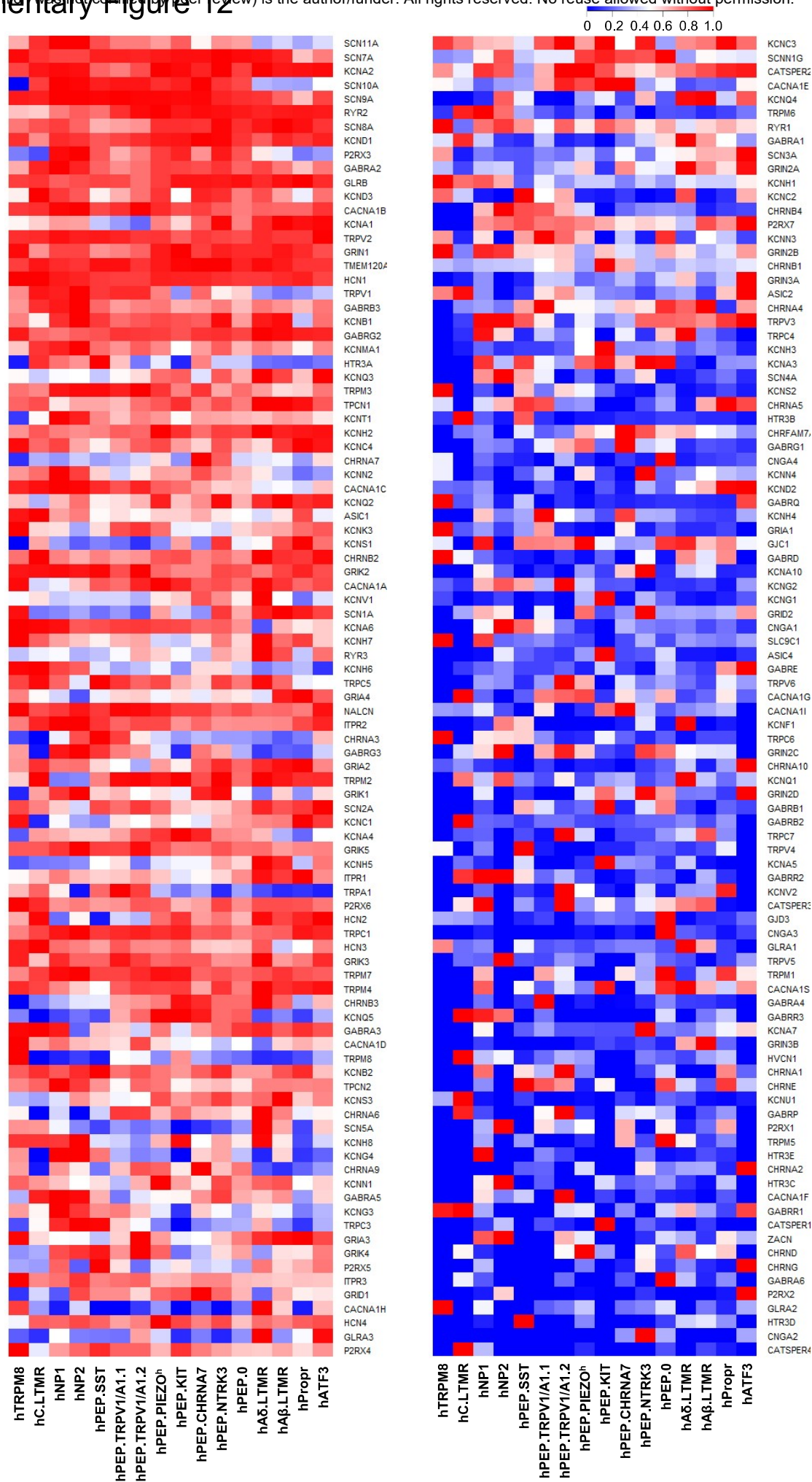
# Supplementary Figure 10



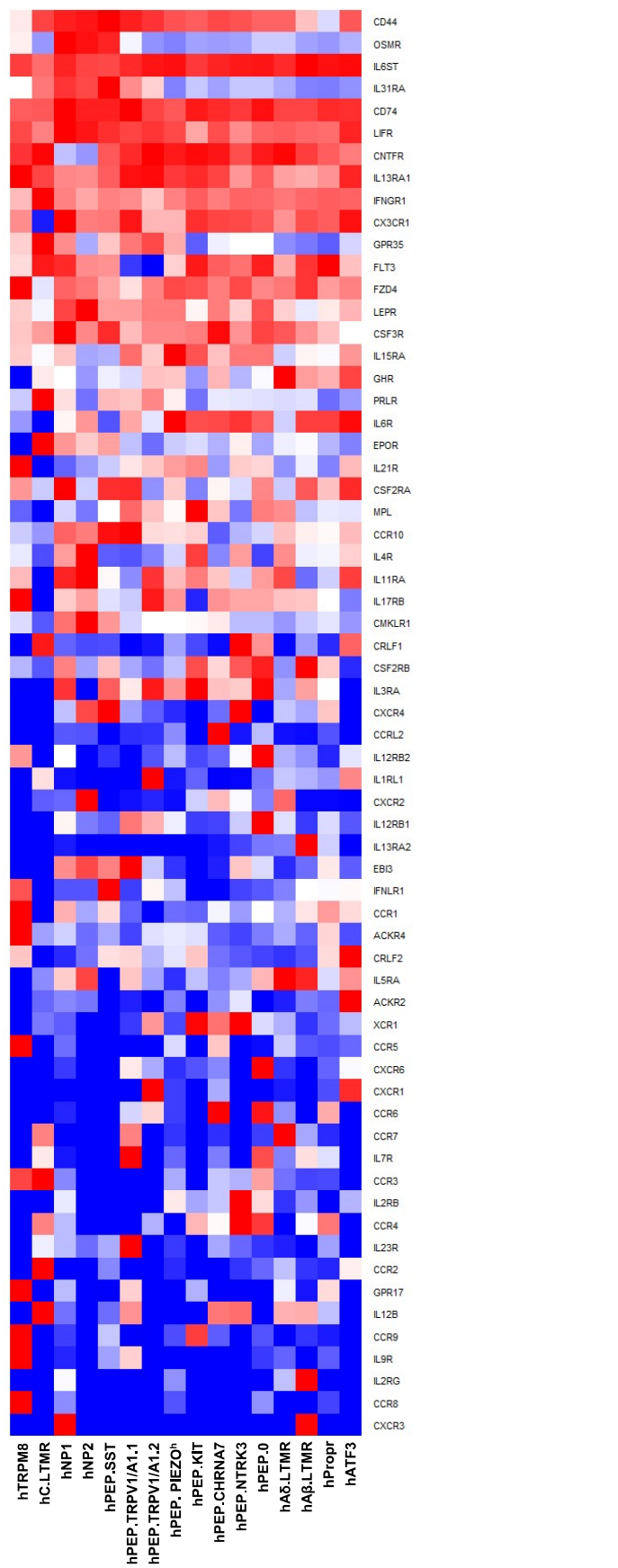
# Supplementary Figure 11



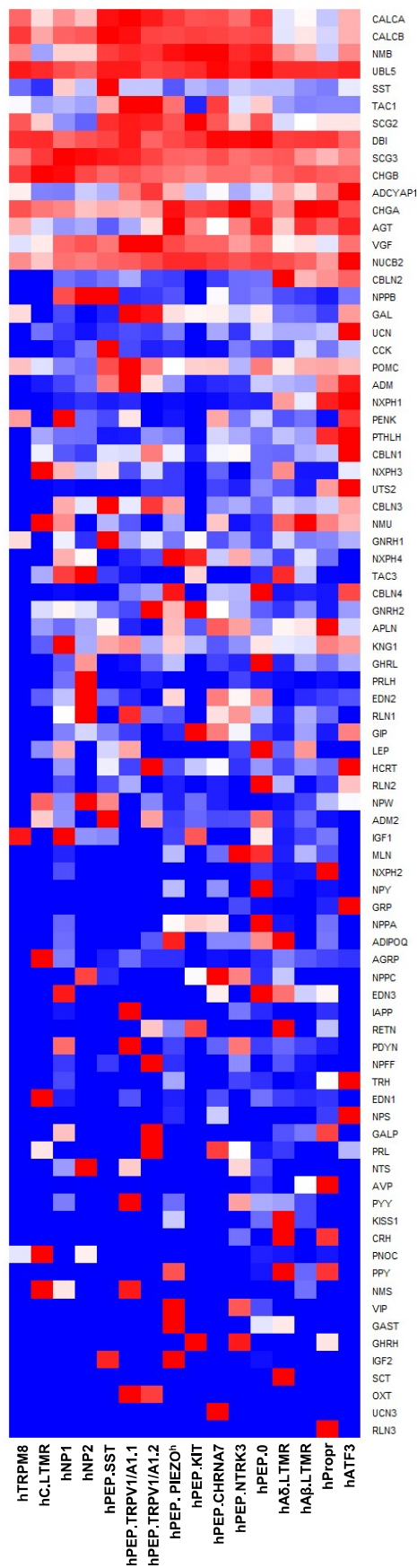
# Supplementary Figure 12



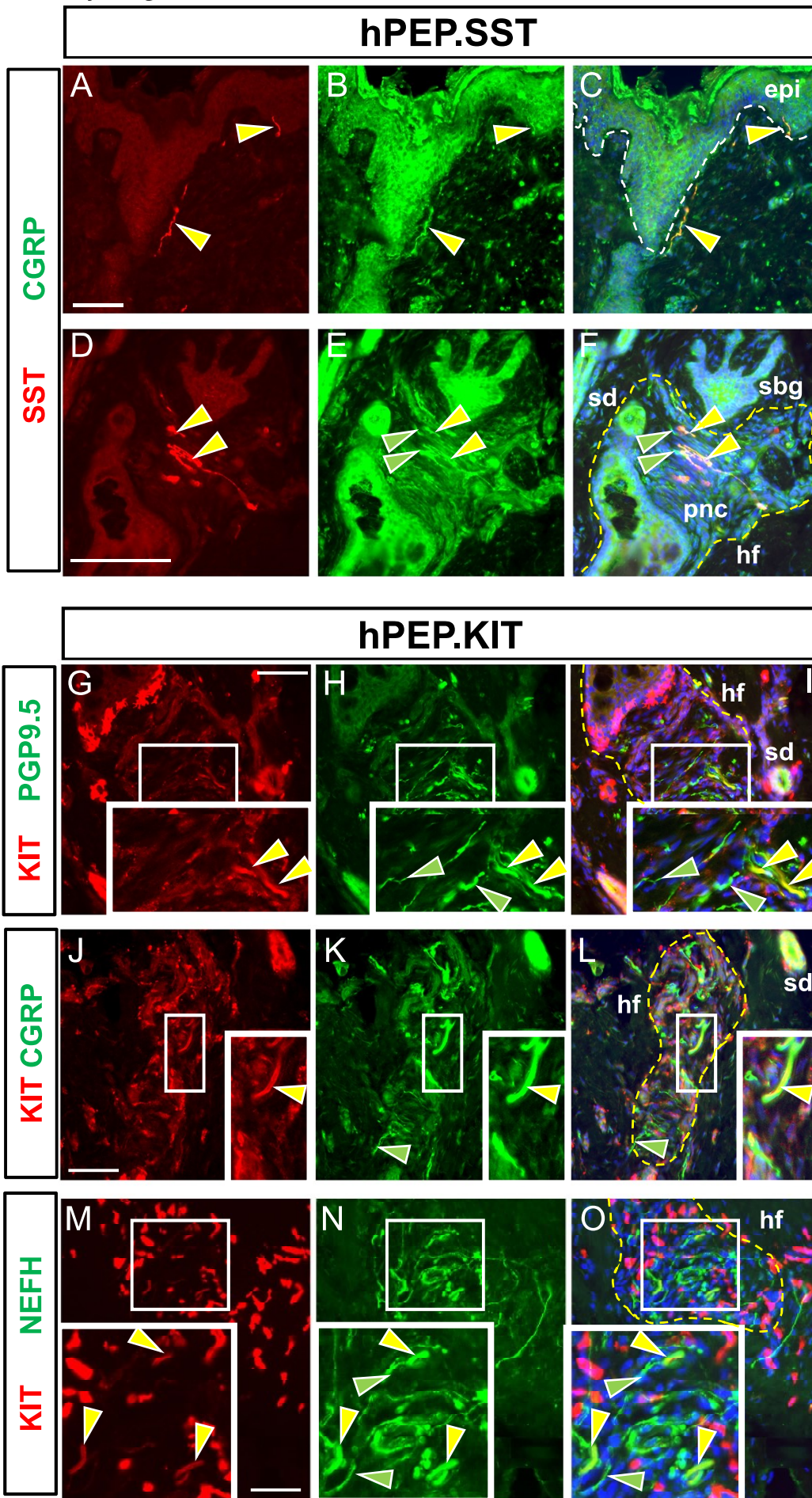
# Supplementary Figure 13



0 0.2 0.4 0.6 0.8 1.0

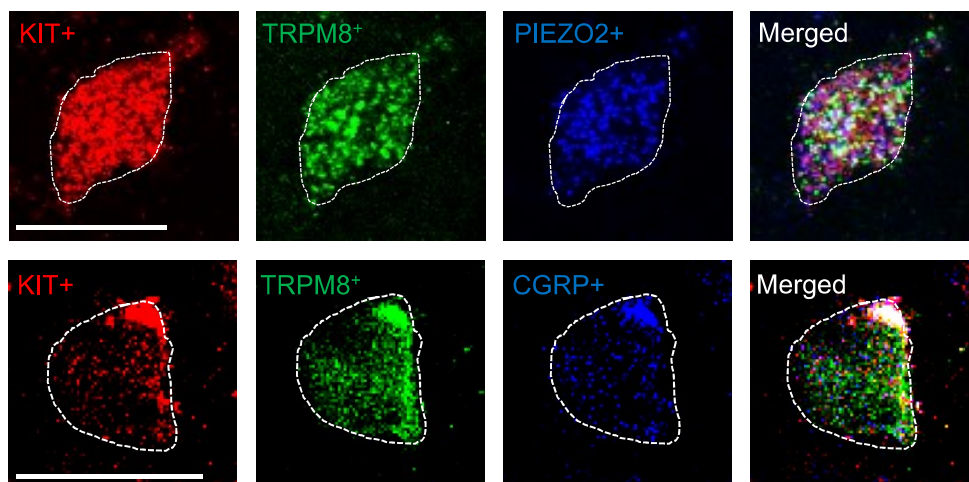


# Supplementary Figure 15

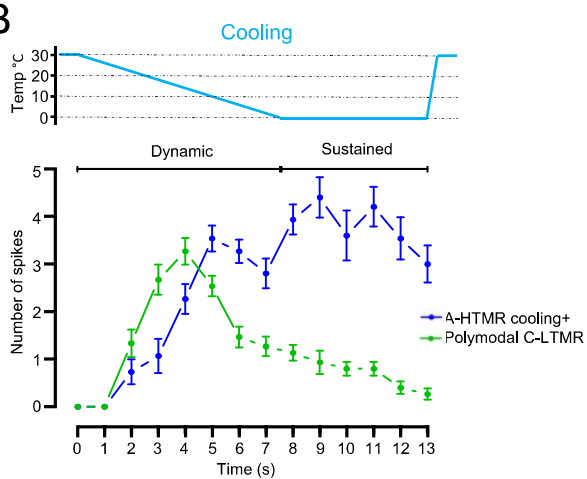


# Supplementary Figure 16

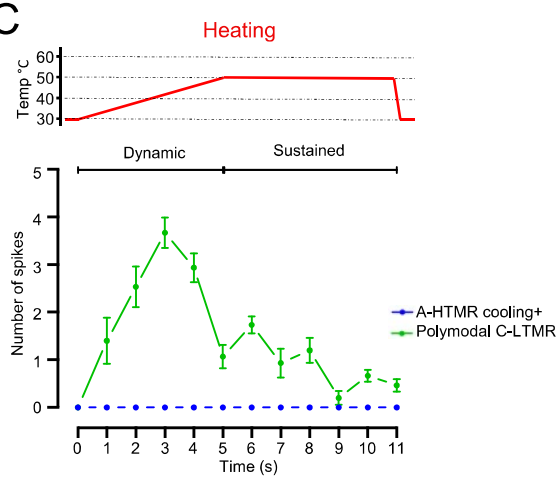
## A hPEP.KIT



## B



## C



# Supplementary Figure 17

